Preliminary Study of a Novel Device for Achieving Drag Reduction on Heavy Road Vehicle

Tak Wing Li

BEng Aerospace Engineering

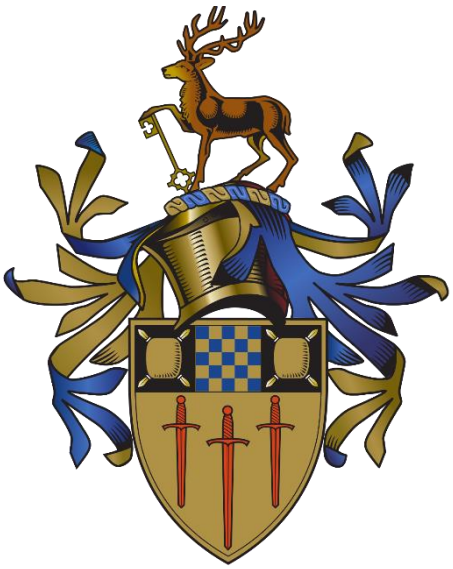

Department of Mechanical Engineering Sciences

Faculty of Engineering and Physical Sciences

University of Surrey

Project Report

May 2019

Project Supervisor: Dr. Eric Lo

Personal Statement of Originality:

I confirm that the submitted work is my own work. No element has been previously submitted for assessment, or where it has, it has been correctly referenced. I have also clearly identified and fully acknowledged all material that is entitled to be attributed to others (whether published or unpublished) using the referencing system set out in the programme handbook. I agree that the University may submit my work to means of checking this, such as the plagiarism detection service Turnitin® UK. I confirm that I understand that assessed work that has been shown to have been plagiarised will be penalised.

Tak Wing Li

Abstract

As the fuel economy in the future gets increasingly more important, the research into more efficient and effective ways to reduce fuel consumption is required. The look into adding drag reduction devices onto heavy vehicles, such as lorries, is one way to be more environmentally friendly, especially with the lorries contributing to 25% of the EU road transport emissions even though they are only a total of 3% of EU's vehicles.

The four models explored in this dissertation consist of: the base model (lorry with a box trailer), lorry with a curved top surface trailer, a boat tail extension at the rear, and a spoiler extension coming off the top trailing edge of the trailer.

The simulations were done in ANSYS Fluent, with the help of meshing in ANSYS ICEM, and used 1:1 2D scale models. The turbulence modelling selected was the standard k-ω with second upwind accuracy used. The grid independence study was done to show the reliable of the mesh and was found that the error was within 4.9%.

Looking at the overall C_D and $C_{L,}$ the curved trailer model was the most ideal at 1.72 and -1.35, respectively. However, looking at the velocity contours and profiles, it says otherwise, with the boat tail and spoiler extension showing less signs of reverse flow and overall drag.

Acknowledgement

I want to start off by giving my gratitude to Dr Eric Lo. Thank you so much for allowing me to take on your project topic even though it was already four weeks in, and also for being so helpful and patient when I needed it. I could not have done this without your guidance.

To all my friends and family members who have told me that I can do this and to continue to push forward, I thank you all for the energy and mentality boosting.

Thank you to my lovely girlfriend, Diana Cheung, for always being there for me and supporting me even though we were both busy!

Special mentions to my friends who were with me for the long periods of time in IFH: Keng Leong Ong, Matthew Law and Colin Chau. We have finally done it!

Contents

List of Figures

Nomenclature

Re_H	Reynolds number	[-]
C_D	Coefficient of drag	[-]
C_L	Coefficient of lift	[-]
C_f	Skin friction correlation	[-]
$\frac{\mu_t}{\mu}$	Viscosity ratio	[-]
$\frac{y}{H}$	Normalised y location	[-]
y^+	Dimensionless wall distance (y-plus)	[-]
y	Wall distance	[m]
H	Height	[m]
n_{nodes}	Node spacing	[m]
A	Surface area	[m^2]
U_∞	Free stream velocity	[m/s]
u_*	Friction velocity	[m/s]
U	X-velocity	[m/s]
Y	Y-velocity	[m/s]
ν	Kinematic viscosity	[m^2/s]
k	Turbulent kinematic energy	[m^2/s^2]
ε	Dissipation rate	[m^2/s^3]
ω	Specific dissipation rate	[1/s]
Ω	Vorticity magnitude	[1/s]
ρ	Density	kg/m^3
τ_w	Wall shear stress	[$kg/(ms^2)$]
α	Slant angle	[°]

1. Introduction

As the future comes, more fuel resources will be used, leaving the total availability to be greatly depleted and the demand for all types of energy resources to be increased; especially fossil fuel such as coal, oil and natural gases. It is predicted that oil will be running out not in the next few hundred years but within most people's life time, in roughly 54 years (Puiu, 2018). That is not a lot of time left.

Others predict to be even sooner, possibly around 2052, which is 33 years from now! The demand for oil has risen to 1.6% which is double the average annual rate for the past decade. At this rate it will only be on an upsurge and has no room to slow down (Cooperativeenergy.coop, 2017).

Although the research into renewable energy sources is one of the highest sought fields currently, it is important to not only rely on the conversion into electric, solar, wind energy etc., but also to look into ways to make the current infrastructures as efficient as possible to support the existing and remaining fossil fuels.

One of the main consumption of fuel nowadays, and for the past decades, have been vehicles. In the EU, lorries account for only 3% of all the vehicles, however looking into the total EU road transport emission this number is a staggering 25%. It is believed that as the years pass by, the fuel needed per engine would be less due to technology improvement. However, looking at figure 1.1, throughout years 1994 to 2014 it can be seen that the fuel consumption is increased (Transportenvironment.org, 2017).

Manufacturer	Model	Year	"Part load" fuel consumption (l/100km)	"Overall" fuel consumption (l/100km)
DAF	FT 85.400 295kW, 11600cc	1996	20	32.9
	XF440 FT 320kW, 10800 cc	2014	20.8	35.6
MAN	19.403 FLS, 294kW, 11967cc	1995	19.9	30.4
	TGX 18.480 353kW, 12419cc	2014	22.7	37.03
Mercedes	1838LS 280kW, 14638cc	1994	24,2	35.8
	1863LS 460W, 15569cc	2014	22,7	35.8
Scania	R113 MA 400A, 295kW, 11000cc	1994	21.4	34.7
	R450 LA 331 kW, 12700 cc	2014	21.78	37.15
Volvo	FH12/340 250kW, 12100cc	1995	23.2	34.7
	FH460 338kW, 12800cc	2014	22.79	37.15

Figure 1.1: Fuel consumption of different manufacturer lorry models between 1994 and 2014 (Transportenvironment.org, 2017).

There are different reasons why fuel consumption have gone up, one reason as shown in figure 1.2, is due to better engines being manufactured over time. Better engines mean more power output but more energy input required.

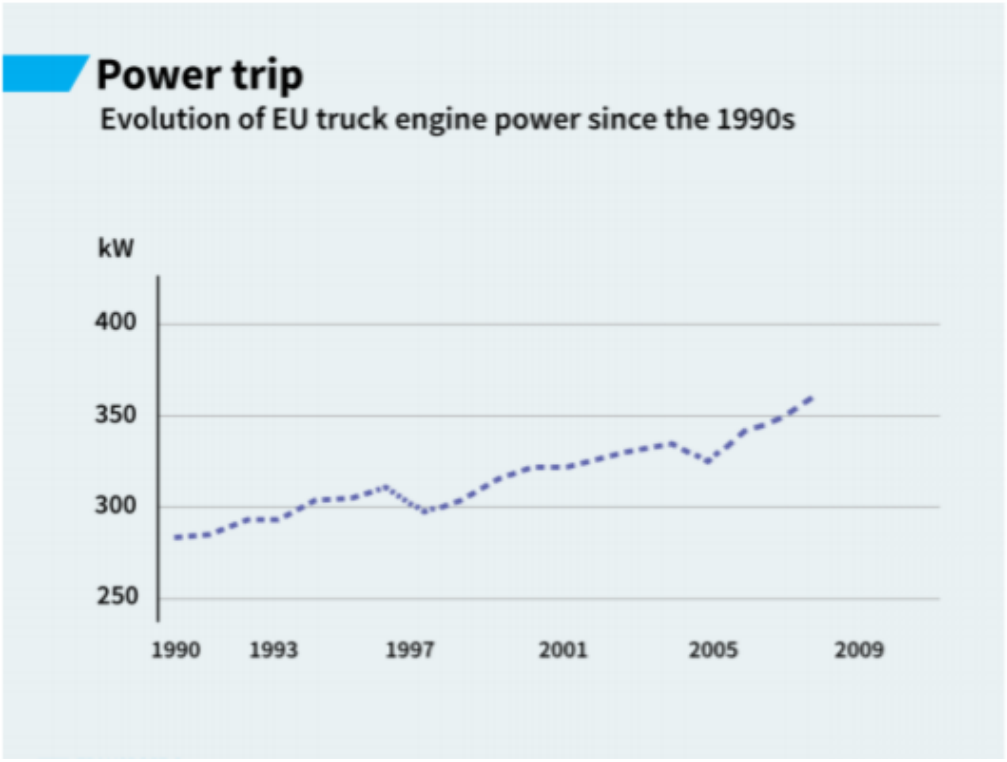

Figure 1.2: Engine power requirement of EU lorries from the 1990s to 2008 (Transportenvironment.org, 2017).

Another reason might be the lack of aerodynamic in lorry structures. Lorries have large surface areas, especially if they have a long backend trailers. This study will look into how varying the shape of the trailer will change the drag on the whole lorry. If the shape can be changed to reduce drag, this means less fuel consumption, more fuel demand met and overall more efficient and economic lorries roaming the roads throughout the whole world.

2. Literature Review

2.1 Flow Separation and the Wake Region

Figure 2.1: Simplified 3D models of a) Ahmed model and b) GM model and their relevance to heavy vehicles (Choi, Lee and Park, 2014).

Through the decades, various number of three-dimensional vehicle models have been investigated to study the effects of the aerodynamics of real vehicles corresponding to their shapes. There are two main models which relate to this study: the Ahmed (Ahmed, Ramm and Faltin, 1984) and the GM model, General Motors (Han et al., 1996). The first model represents a fast-back vehicle and the second model represents a square-back vehicle (Figure 2.1). In the Ahmed model, the rear section composes of a rear slanted surface which enables the study of the effect in a variety of rear shapes. Whereas, the GM model has a flat square back with a sharp trailing edge. The common feature in both models is that they have a rounded front body to prevent the flow stream to separate when it comes in contact to the edge. The main bodies are rectangular cross sections which means that after the flow passes the front, it would develop into a turbulent boundary layer until it meets the trailing edge which causes the flow to separate off. Although the Reynolds number of the Ahmed and GM models Re_H = 1.18 x 10^6 and 1.7 x 10^5, respectively, are lower than that of a typical tractor-trailer, shown in this study, the wake regions should show similar characteristics.

In 1984, the effect of the rear slant angle on the aerodynamic drag was investigated by Ahmed et al., the time-averaged flow structures of the wake present taken as the slant angle, α, was changed. It was shown that there are two separate flow separation regimes. Firstly, when $0° < \alpha \leq 12.5°$, the flow would separate at the rear edge and as the slant angle increase, the drag would decrease. The second region, $12.5° < \alpha \leq 30°$, has the opposite effect on the drag, as the slant angle increases, drag will also increase. In terms of the flow, the flow in the second regime, separates the front edge of the slanted surface but immediately reattaches to form a small recirculation bubble (Shown in figure 2.2). The size of the bubble also increases with slant angle. The main source of the drag is due to the pair of counter-

rotating longitudinal vortices which form along the side of the slanted edges, this is known as the induced drag (Hucho and Sovran, 1993; Minguez, Pasquetti and Serre, 2008).

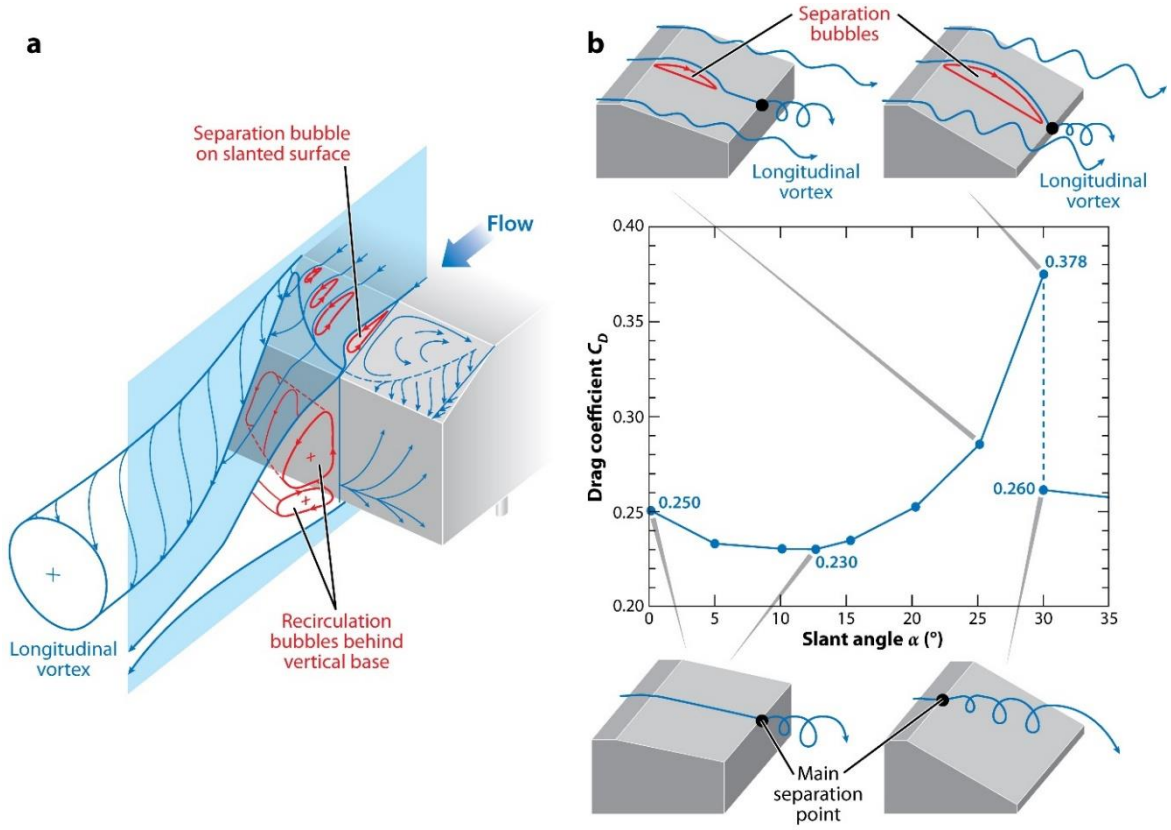

Figure 2.2: The aerodynamics of a flow over the Ahmed model. A) Time-averaged 3D flow structures in the wake region. B) The coefficient of drag versus the slant angle, α. (Choi, Lee and Park, 2014; Ahmed et al., 1984)

At the slant angle of α = 30°, the critical angle, both regimes of high and low drag can exist. In high-drag, the flow reattaches right before the vertical base after being separated at the front edge of the slope. The induced drag increases even further as the longitudinal vortices created from the side edges of the slanted surface at this stage reaches a maximum. During the low-drag regime, the recirculation bubble lying on the slanted surface and the longitudinal vortices disappear, and just the flow separated from the trailing edge remains (Choi, Lee and Park, 2014).

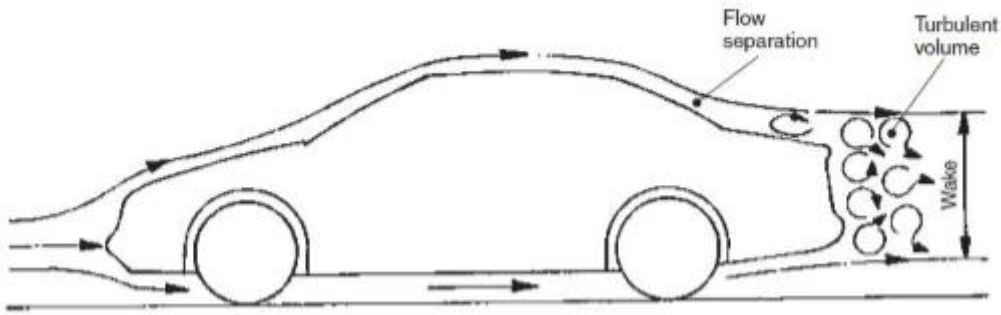

Figure 2.3: Flow separation and wake region of passenger car (McNamara, 2018)

Once flow separation at the rear edge of the vehicle occurs, the wake region is formed, along with the upper and lower shear layers. The width of this region depends on the Reynolds number; at small Reynolds, the boundary layer (BL) is laminar and the flow separation would have occurred at the maximum height of the BL thickness. The resulting wake region behind the vehicle is broad. However, at the critical Reynold's number, $Re_{H,crit} = 5 \times 10^5$, the BL transitions from laminar to turbulent and the wake region becomes narrow. The drag coefficient, defined in equation 1, is lower for sub-critical Reynolds numbers. For the drag to be the lowest as possible, the flow should be attached as long as possible for the pressure rise to be as large as possible (Ahmed and Hucho, 1998).

$$C_D = \frac{D}{\frac{1}{2}\rho {U_\infty}^2 A} \tag{1}$$

In the wake region the existence of wake vortexes, formed by the coiling up or down of upper and lower shear layers (Lo and Kontis, 2017), are likely and these behave in different manners depending on the type of flow separation.

In the first case where the separation line may be located perpendicular to the flow direction (shown in figure 2.4 by the bluff body), the flow is unsteady and the kinetic energy of the vortex fields rapidly dissipate by the turbulent mixing and frictional heat is produced. This causes a large total pressure loss in the overall wake region, which increases the drag considerably due to the inability to overcome the pressure drags easily.

In the second type of flow separation where the body is inclined with respect to the oncoming flow (shown in figure 2.4 by the streamlined body), the flow separation is more steady and well-ordered. This leads to a smaller total pressure loss and allows the necessary amount of kinetic energy to overcome the pressure drag (Ahmed and Hucho, 1998).

With previous experiments, it has been shown that these wake vortexes show different behaviour if the wheels are stationary or rotating. In stationary wheels, the vortexes are stronger than in the case of rotating wheels, due to the stronger downwash (Axerio-Cilies, 2012). It also has been shown that the tendency of the vortexes to stay close to the ground was found in stationary wheels and in rotating wheels tend to situate 0.25 times the height of the lorry (Bearman et al., 1988).

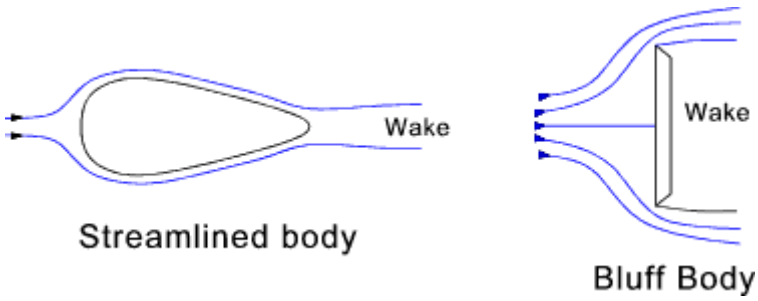

Figure 2.4: Flow separation on streamlined and bluff bodies (Beardmore, 2013).

2.2 Drag Reduction Devices

Standard tractor-trailer lorries, i.e. box shaped cabin and trailer, generally have high drag. There are multiple drag-reduction devices available to reduce the overall drag. There are 3 main areas of the lorry the drag is developed from: the forebody, rear body (base) and the underbody. The aerodynamic drag accumulated from the forebody is approximately 25% at the front of the face and 20% for the gap in between the cabin and the trailer. From a typical tractor-trailer, the trailer base contributes to 25% and the remaining 30% is from the underbody flow (Choi, Lee and Park, 2014). In earlier attempts to increase fuel economy, companies had increased the radii of the corners and edges to delay the flow separation. It was reported that in a full-scale test, the fuel savings were 20%, when these changes were used (Steers and Saltzman, 1977).

For the forebody, there are many available drag reduction methods, however the two main devices used are the cab deflector (shown in figure 2.5 & 2.6) (Cooper, 2003; Leuschen and Cooper, 2009; Malviya, Mishra and Fieldhouse, 2009) and the cab side extender (figure 2.4) (Castellucci and Salari, 2005; Cooper, 2003; Hyams et al., 2011; Storms et al., 2004). The side extender is a good way to delay flow separation at the leading edge so that the low-pressure region is displaced further away from the trailer base. At normal operating conditions, lorries generally run on motorways which the aerodynamics would vary according to crosswind conditions and the cab deflector provides the largest drag reduction of approximately 20% at zero yaw angle, but this reduction decreases as the yaw angle increases (Choi, Lee and Park, 2014).

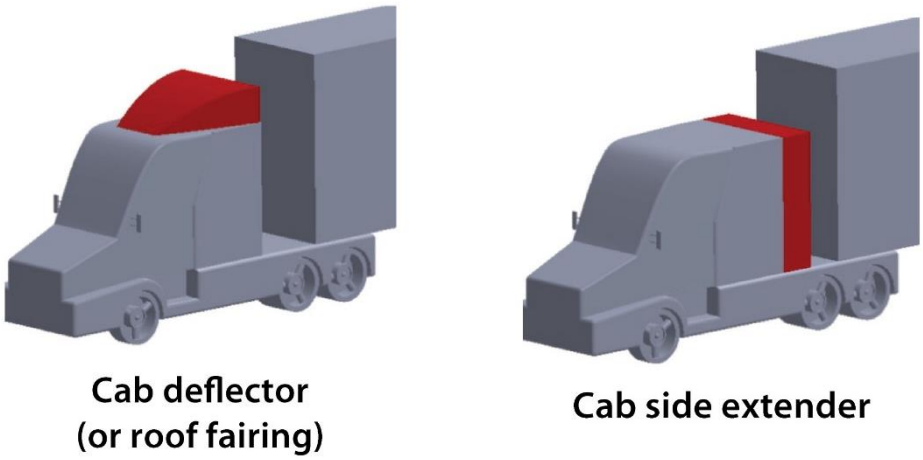

Figure 2.5: Lorry with drag reduction devices, left showing cab deflector and right showing cab side extender (Choi, Lee and Park, 2014).

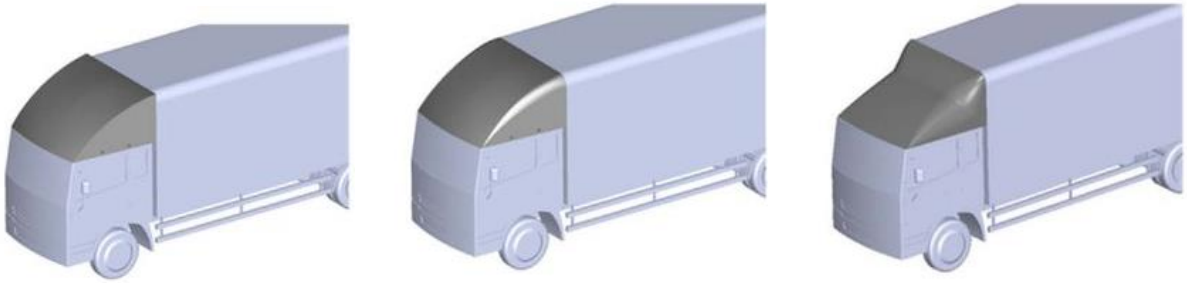

Figure 2.6: Different modifications of cab deflectors with streamline curvature based (left), rounded edges (middle) & combination of both at a more shallow slope angle (Kim et al., 2015).

For the base drag reduction of square back vehicles, which relate to this study, the flow separation is fixed at the sharp trailing edge. This leads to a large recirculation bubble in the wake which drops the base pressure, increasing the drag, and to counter-act this phenomenon it is best to shift the bubble away from the rear or to reduce its size (Balkanyi, Bernal and Khalighi, 2002; Englar, 2001; Gilliéron and Kourta, 2009; Howell, Sheppard and Blakemore, 2003; Littlewood and Passmore, 2012; Peterson, 1981; Wong and Mair, 1983; Yi, 2007).

The best devices in terms of effectiveness and practicality for drag reduction have been seen to be base cavities and boat tails (shown in figure 2.7). In both devices, they push the recirculation bubble downstream and delay the flow separation which in return reduces the size of the bubbles. They also help by deflecting the moving flow inwards towards the main body from the trailing edge (Balkanyi, Bernal and Khalighi, 2002; Khalighi et al., 2001; Verzicco et al., 2002; Yi, 2007). Later on in this study, the boat tail model shall be investigated. It can be shown that the flow separation is split into 3 regimes, 3 behaviours. The second regime, where $5° < \alpha \leq 15°$, is where the lowest coefficient of drag lies. The separation bubble is formed at the leading edge of the boat tail and a strong near-wall momentum after the flow reattaches to the surface, delays the separation to the trailing edge, which results in the most significant drag reduction. In figure 2.8, the lowest value of C_D has been investigated to be $\alpha = 15°$ (Choi, Lee and Park, 2014).

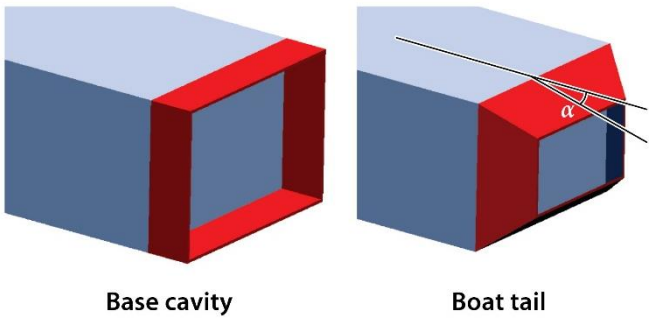

Figure 2.7: Drag reduction devices, base cavity (left) and boat tail (right) (Choi, Lee and Park, 2014).

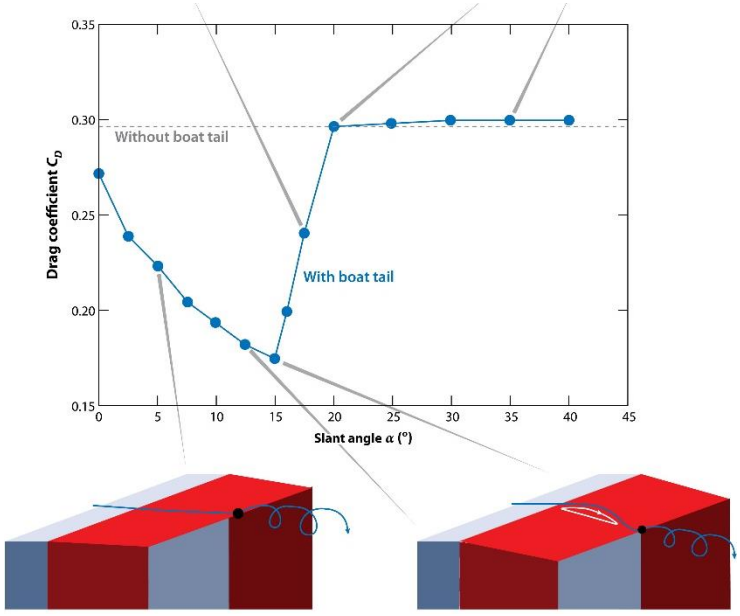

Figure 2.8: The variation of C_D at different slant angles of the boat tail (Yi, 2007; Choi, Lee and Park, 2014).

For the underbody drag reduction, little investment has been made to control the flow underneath the heavy vehicles. The suggested devices which have been previously tested are the undercarriage skirts (Buil and Ferrer, 2009; Cooper and Leuschen, 2005; McCallen et al., 2005; Ortega and Salari, 2004; Raemdonck and Tooren, 2009), belly boxes (Cooper and Leuschen, 2005; Storms et al., 2004), and undercarriage wedge skirts (Cooper and Leuschen, 2005; Ortega and Salari, 2004). (All shown in figure 2.9). The straight skirt has been shown to block lateral flow that comes beneath the trailer body, which means as the yaw angle increases, so does the ability to reduce drag. Its performance is null when it comes to zero yaw angle. To try to fix this problem the wedge skirt was created, but it has been found to only provide drag reduction at lower yaw angles, close to zero (Ortega and Salari, 2004). The belly box as an alternative, provides a wheelhouse to enclose the tire as well as blocking lateral flow. The drag reduction has been calculated to be around 38% (Storms et al., 2004).

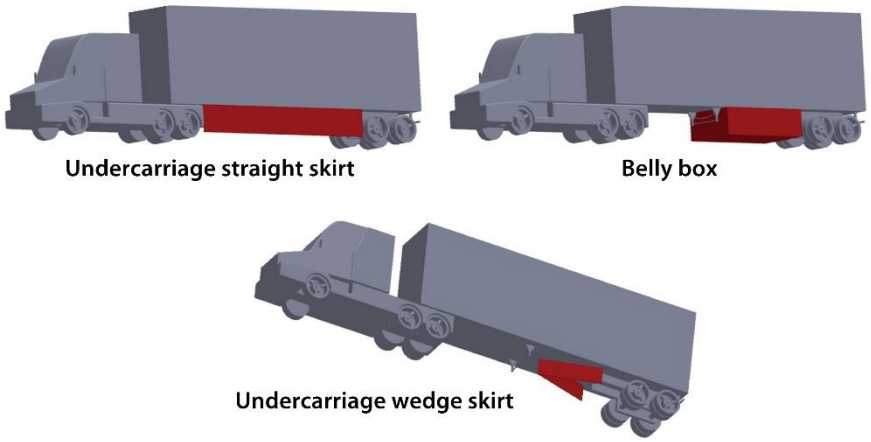

Figure 2.9: Devices for drag reduction in the underbody of the tractor-trailer (Cooper and Leuschen, 2005; Choi, Lee and Park, 2014).

2.3 Turbulence Models

In computational fluid dynamics, it is important to select a turbulence model to calculate the fluctuating velocity fields which characterise the turbulent flows. In reality it is really expensive to computationally simulate directly in practical engineering calculations due to the multiple fluctuation quantities such as momentum, energy, and the species concentrations. Instead, certain sets of governing equations can be used as a time-averaged calculation to remove the small scales, resulting in a modified set of equations which are a lot cheaper to compute (Fluent Inc., 2003).

There are two main methods in solving turbulence flows: Reynolds-averaged Navier-Stokes (RANS) or large eddy simulation (LES) methods. In RANS, the equations represented are for the time-mean flow quantities only and can be used in all scales of turbulence. If the flow is steady, no time derivatives will be contained and a steady economical solution is obtained. Whereas in LES, the large eddies or vortexes generated are computed in a time-dependent simulation that uses filtered equations. In these filtered equations, the small eddies smaller than the set size are filtered out. The advantage of this is to solve less turbulence and solve more of the other flow, reducing the error induced by turbulence (Fluent Inc., 2003).

In this study, it was thought that the turbulence induced won't be large enough to cause problems in the simulation so the LES method was disregarded and a model from the RANS method was chosen instead. The other benefit of this was that it would decrease the computational costs per iteration.

There are a few RANS based models: the one equation based, Spalart-Allmaras and the two equations based which compose of the standard k-ε, RNG (renormalized group) k-ε, realizable k-ε, standard k-ω, SST (shear stress transport) k-ω and Reynolds stress model. The three standard models which will further be explained are the Spalart-Allmaras, standard k-ε and standard k-ω (ANSYS Inc., 2006).

In the Spalart-Allmaras model, it is a low cost RANS model for solving modified eddy viscosity. When in this form the eddy viscosity is easy to solve near the wall. It was designed mainly for aerospace applications involving wall-bounded functions and has been shown to give good results at adverse pressure gradients. The near-wall gradients in this model are much smaller than the gradients in the k-ε and k-ω models, leading to less sensitivity to numerical errors. Although the benefits sound good, this model is still relatively new and there are no claims that it can be used in all types of complex flows (ANSYS Inc., 2006; Fluent Inc., 2003).

In standard k-ε, it is the most used model in industrial applications due to its robustness and accuracy. Within the model, there are sub models which take into account the compressibility, buoyancy, combustion and other aspects of the flow. However, there are two main limitations to this model. Firstly, the ε equation contains a term which does not allow it to be solved at the wall and therefore a wall function must be used. The other downside is that if the flow separation is too strong, the streamline curvature is large or the pressure gradient is too big, then the model performance will be poor (ANSYS Inc., 2006).

The standard k-ω model in FLUENT is based on the Wilcox k-ω (Wilcox, 1998), this model has gained more popularity throughout the years because the equations in it do not contain terms which are undefined at the walls, meaning it can be integrated without use of wall functions. Compared to the other two, it is more accurate and robust for a wider range of boundary layer flows with pressure gradient. It is also used in aerospace and turbo-machinery communities. As in k-ε, it also has sub models which take into account the low-Reynolds number effects, compressibility effects, transitional flows and shear-flow corrections (ANSYS Inc., 2006).

2.4 Reynolds Number in Scaled Models

In CFD and wind-tunnel simulation it is important that the scale of the model being tested is suitable enough so that the results of the replica can be used reliably in real world scenarios without major errors. Although this study will be using CFD simulations, it is still important to address the correct scaling, in case of future work in wind tunnel testing.

The main reason scaled models are used is so that models of large vehicles or bodies of objects can be recreated and fitted into wind tunnels. It is unreasonable to fit a 15 metre long lorry into a wind tunnel. The Reynolds number is shown in equation 2 (Ahmed and Hucho, 1998):

$$Re_H = \frac{U_\infty H}{\nu} \tag{2}$$

The problem with reducing the scale of a model is that if the height changes, and results in a reduction in the Reynolds number. To maintain the same Reynolds number in the small scale as in the original sizing, the free stream velocity would have to increase. However, looking at (1), the coefficient of drag would be affected. By increasing the velocity, the C_D value would drastically decrease. In terms of the flow type, although the overall flow might be turbulent, if looking at a smaller part of the vehicle the

flow might be laminar, due to the smaller scale sizing. It is therefore important to find a scale sizing which is large enough to reproduce all the needed geometrical details and the Reynolds number is independent of the coefficient of drag, meaning there won't be problems of running into Mach number problems (Ahmed and Hucho, 1998).
As tested in previous studies (shown in figure 2.9), the influence of Reynolds number on drag starts to become less as the scale go from 1:10 to 1:2.5. At 1:2.5 scale it is known to achieve the most reliable results, shown by the flat gradient in the graph indicating little fluctuation and change of C_D.

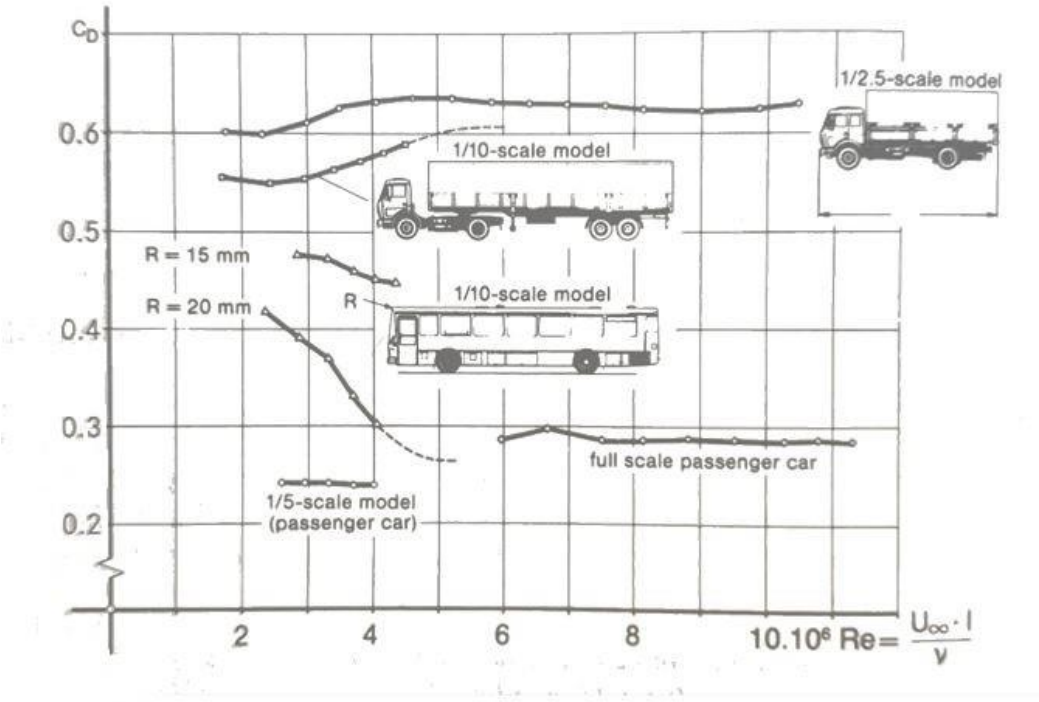

Figure 2.10: Influence of Reynolds number on drag (Ahmed and Hucho, 1998).

Due to the simulation in the study being in CFD, it is very possible and more reliable to use 1:1 scale model to produce the best results.

3. Two Dimensional Computer Aided Design Models

The first stage of the study were to create the models necessary for the simulation. Solid Edge ST10 was the chosen software as it was the most accessible and available program.

The supervisor supplied the 1:20 scale 3D model of the lorry which is based on the MAN TGX Euro 6**.** From there, 4 different lorry configurations, specifically the shape of the trailer, were created using the tools in the software. The figures below show the dimensions of the 1:1 scaled up models of the box trailer, curved trailer, boat tail end curved trailer and the curved trailer with a spoiler.

Each model were exported as a .STL file for use in the meshing stage.

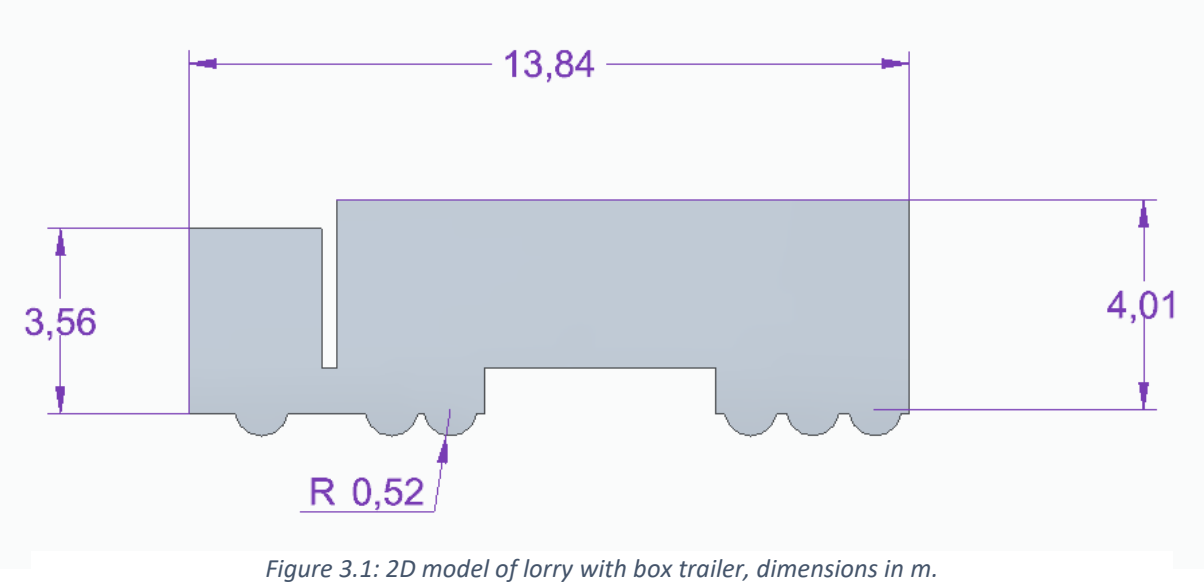

Figure 3.1: 2D model of lorry with box trailer, dimensions in m.

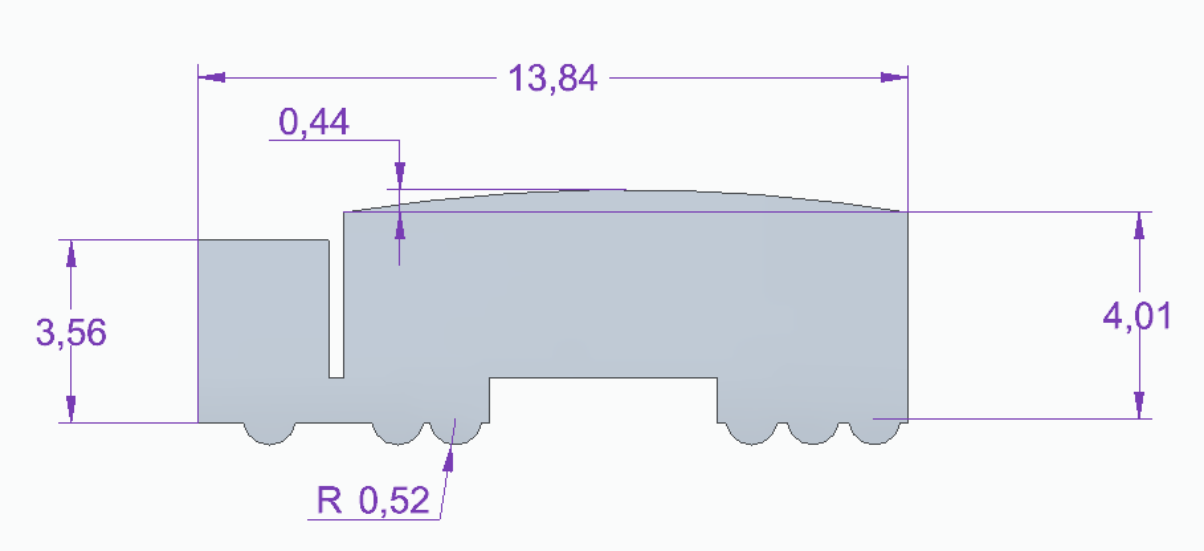

Figure 3.2: 2D model of lorry with curved trailer, dimensions in m.

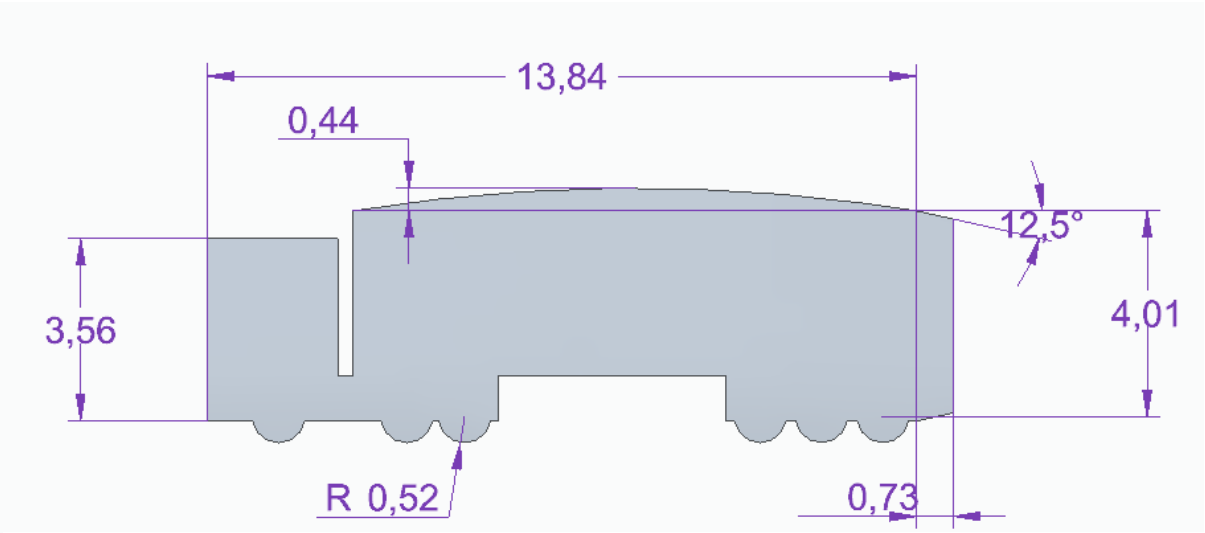

Figure 3.3: 2D model of lorry with boat tail curved trailer, dimensions in m.

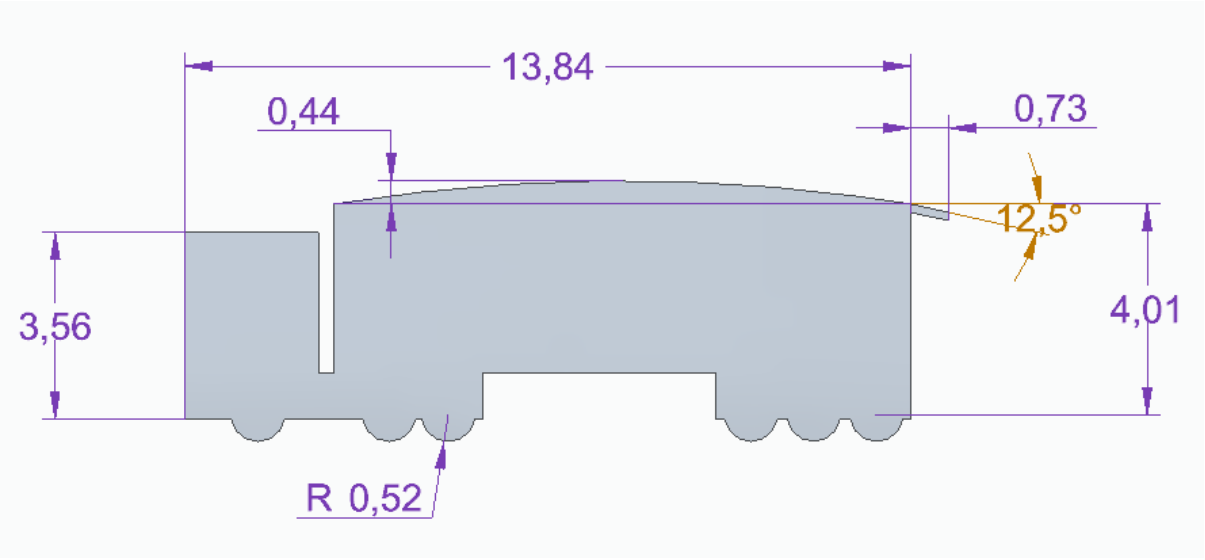

Figure 3.4: 2D model of lorry with curved trailer ending with spoiler, dimensions in m.

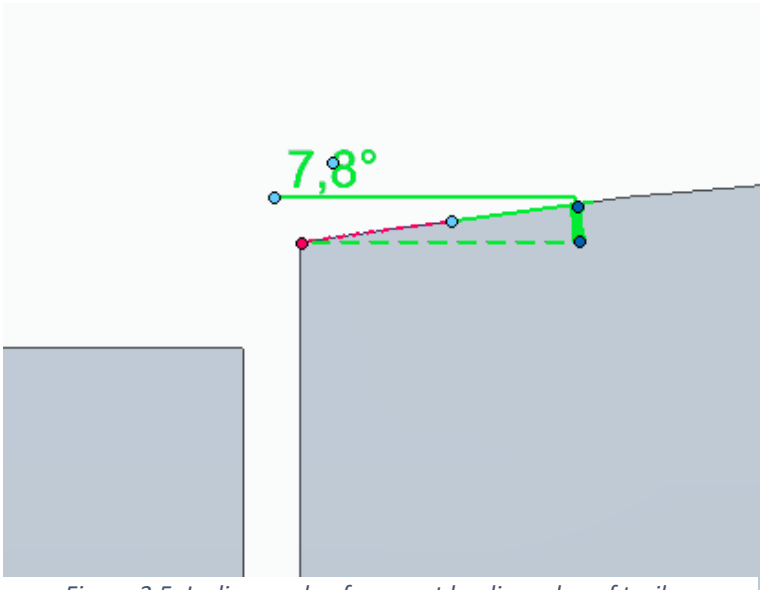

Figure 3.5: Incline angle of curve at leading edge of trailer.

4. Computational Fluid Dynamics

4.1 Software Introduction

The two main computer software used in this study are ANSYS ICEM and ANSYS FLUENT.

ANSYS ICEM allows the meshing of large or complex models in both 2D and 3D. It is capable of producing structured or unstructured meshes and allows the user to adjust the meshing with ease once the basic learning of the program has been achieved.

ANSYS FLUENT is a software made to model different types of flow on any imported model (as long as it is supplied as a mesh). These flows can be laminar or turbulent. Different parameters, such as drag, lift, heat transfer, velocity changes etc. can be measured and the program can output these into external files to allow users to plot as graphs or to calculate time averaged values. This software eliminates the need for a real life wind tunnel to simulate real life scenarios, in this studies case being a cruising lorry.

By using ANSYS Workbench, the two programmes can be easily linked and any changes in the mesh in ICEM will prompt the user to update the upstream data to FLUENT so that the new mesh can be imported, used in the calculations and new chosen values can be obtained.

4.2 Reynolds number

As explained before in section 2.3, it is important to know what type of turbulence modelling would be needed in the simulation and for starters one of the biggest factors is whether or not the model under the specified conditions is a low or high Reynolds number model.

The Reynolds number Re_H, of the flow on the lorry with the previous stated conditions were calculated using (1) and where ν, the kinematic viscosity, is defined in Equation 3 (Ahmed and Hucho, 1998) as:

$$\nu = \frac{\mu}{\rho} \tag{3}$$

The dynamic viscosity and density were according to the atmospheric values at sea-level:
μ= 0.000018375 kg/(ms) and ρ=1.225 kg/m^3.
The height, H, of the reference model being 4.52 m, the Reynolds number can be calculated as
$Re_H = 8.14 \times 10^6$.
This value is similar to a typical tractor-trailer lorry of ~ 9×10^6 and also previous studies through experimental (Haff et al., 2009) and numerical (Castellucci and Salari, 2005) approaches used Reynolds number between 1×10^6 and 7×10^6. Although both the Reynolds number calculated above and previous study values are smaller than the typical operating number, which classified the lorry for this study to be a low Reynolds number model, it would be appropriate as the coefficient of drag is independent of the Reynolds number greater than 10^6 (Choi, Lee and Park, 2014).

4.3 ANSYS ICEM

4.3.1 Setup

To start the whole meshing process, the model was imported in as a geometry (.STL file) and points were plotted around the shape for it then to have curves connected between them to recreate the model. The reason the .STL file could not be used is because it is technically a 3D model due to it being assigned 1mm thickness so that the model could have a body to be saved as the file. Hence, a new sketch was created around it and then the imported geometry was removed.

A region was created to act as the wind tunnel for the lorry. The coordinates in metres are:

A(-60, 61), B(120, 61), C(-60, 0.12) & D(120, 0.12)

These locations are shown in figure 4.1, along with the origin (0,0) location.

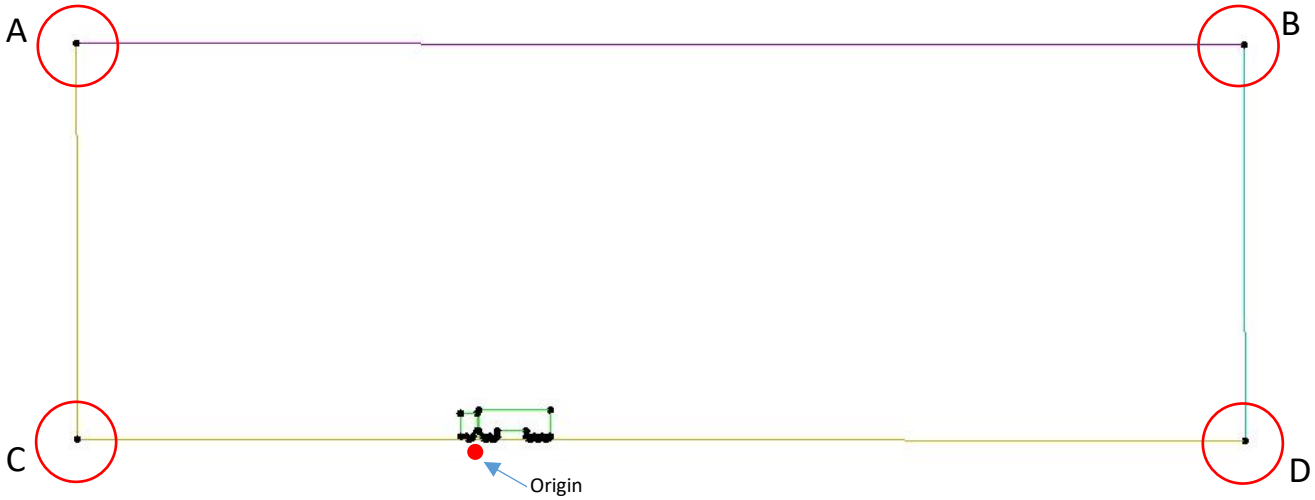

Figure 4.1: Full domain of ANSYS ICEM setup.

4.3.2 Blocking & Association

In order for FLUENT to detect the edges of the lorry, blocking and associating a domain to the lorry is needed.

For all the models, the number of nodes for each edge are almost identical and they also have a near wall o-grid of 0.3m. In the below figures, it shows how the blocking looks like and how it fits around the lorry. A close up at the wheel locations show how the blocking was made to curve with the wheel. This was done using the “Automatic Linear” and “Link Edge” functions on the program.

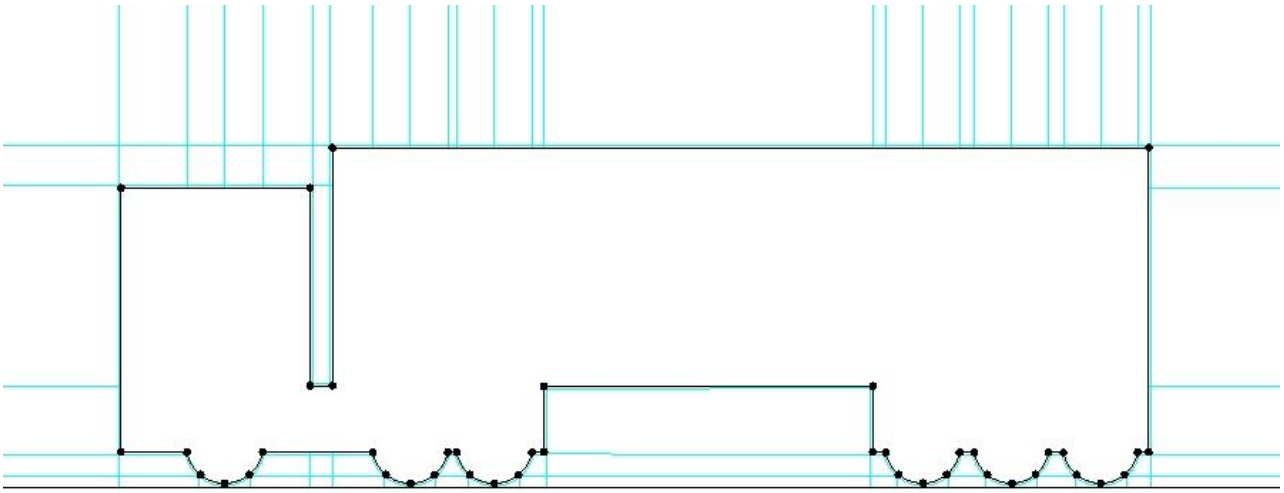

Figure 4.2: Full blocking setup around the lorry.

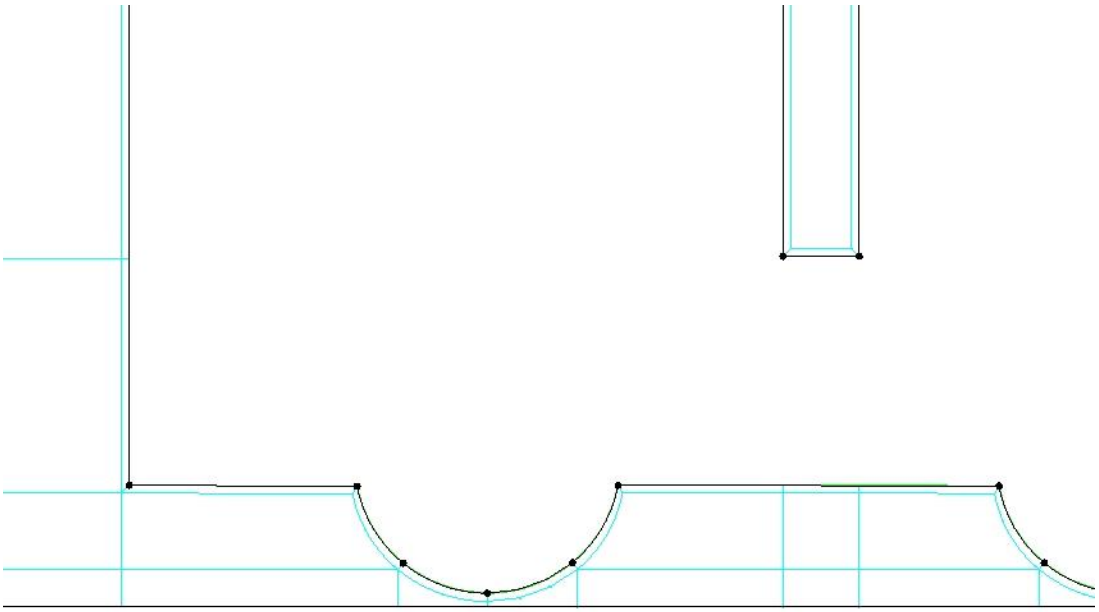

Figure 4.3: Close up of blocking around the wheel.

The total number of nodes for each model are the following:

Box trailer = 186k

Curved trailer = 194k

Boat tail trailer = 197k

Spoiler trailer = 209k

The limit of total number of nodes allowed to be used in ANSYS Fluent is 500k. This was due to the licensing currently available for the students.

Later on in section 4.5, the node numbers for one selected model (in this study the box trailer model), were changed three more times to allow the study of grid independence.

4.3.3 Y-Plus Wall Distance

In order to get a reliable simulation result from the mesh in FLUENT, the near wall distance including the y-plus had to be calculated and factored in. There are 5 main procedures in calculating the node spacing: the Reynold's number, skin friction, wall shear stress, friction velocity and then the node spacing. The first stage is to obtain the Reynold's number (2), which afterwards is used for the Schlichting skin friction correlation shown in equation 4 (Rodríguez, 2014):

$$C_f = [2log_{10}(Re_H) - 0.65]^{-2.3} \quad \text{(for } Re_H < 10^9\text{)} \tag{4}$$

Using this skin friction value, the wall shear stress can be calculated with equation 5 (Rodríguez, 2014):

$$\tau_w = C_f \frac{\rho {U_\infty}^2}{2} \tag{5}$$

Using this correlation, the friction velocity can be related with the following equation 6 (Rodríguez, 2014):

$$u_* = \sqrt{\frac{\tau_w}{\rho}} \tag{6}$$

The last step to work out the near wall spacing, is to find the linear sublayer thickness using equation 7 (Rodríguez, 2014). This equation involves a new parameter of y+ which is the y-plus desire, the closer to 1, the better and more accurate the outcome results would be.

$$y = \frac{y^+ \nu}{u_*} \tag{7}$$

In order to work out the individual node spacing in the linear sublayer, a small modification to equation 8 above can be made as shown in the following (Rodríguez, 2014):

$$y = \frac{y^+ \nu}{n_{nodes} u_*} \tag{8}$$

However for ease, an online y-plus calculator was used to speed up the calculation process instead of having to manually input the numbers into the formulas each time.

The initial desired y-plus selected was set to 1, however the wall spacing it outputted was too small and the calculation would not converge in FLUENT. Therefore, after a few tries, it was determined that

the minimum desired y-plus value was 5. The reference length that the calculator refers to is the height of the lorry. The total wall spacing equals to 7.6 x 10^{-5} m, which also matches the theoretical value using the equations above. Since both the theoretical and automated values are equal then it can be said that the y-plus calculator is reliable.

4.3.4 Mesh

After the blocking stage, an unstructured mesh was generated to be inputted into ANSYS Fluent. The decision to use unstructured instead of the popular option of multi-block structured mesh was due to the initial idea that this study was to look into the three-dimensional aspect of the lorry to analyse more realistic and useful data. However, due to the limited total number of cells allowed in FLUENT, it was decided that this study would continue with only looking into the 2D models. Both methods of the meshing work, unstructured meshing offers more flexibility to 3D models but this does not mean for 2D models it would not work out. Multi-block offers a higher numerical accuracy and less computer storage. In this study the blocking was not too complex so the idea of multi-block is definitely feasible, however choosing unstructured meshing was also allowable (Ali, Tucker and Shahpar, 2016).

As shown below in figure 4.4, the regions away from the main lorry body have a coarse sized mesh, this is due to the flow being uniform in those areas. In figures 4.5 and 4.7, there were a denser mesh surrounding the close proximity of the lorry, and especially the near wall where there is a thin but highly fine mesh region around the whole perimeter of the model.

The maximum cell size chosen for each part of the domain (i.e. the lorry, the fluid, inlet, outlet, top and ground) was 0.5 metres. This kept the total node numbers to be below 500k but not too low for the mesh to be considered coarse. The average total node number, shown in section 4.3.2, was seen to be around 190k. This meant that the maximum cell size could have been slightly less, to increase the numbers closer to 500k, but it would mean more processes to be computed.

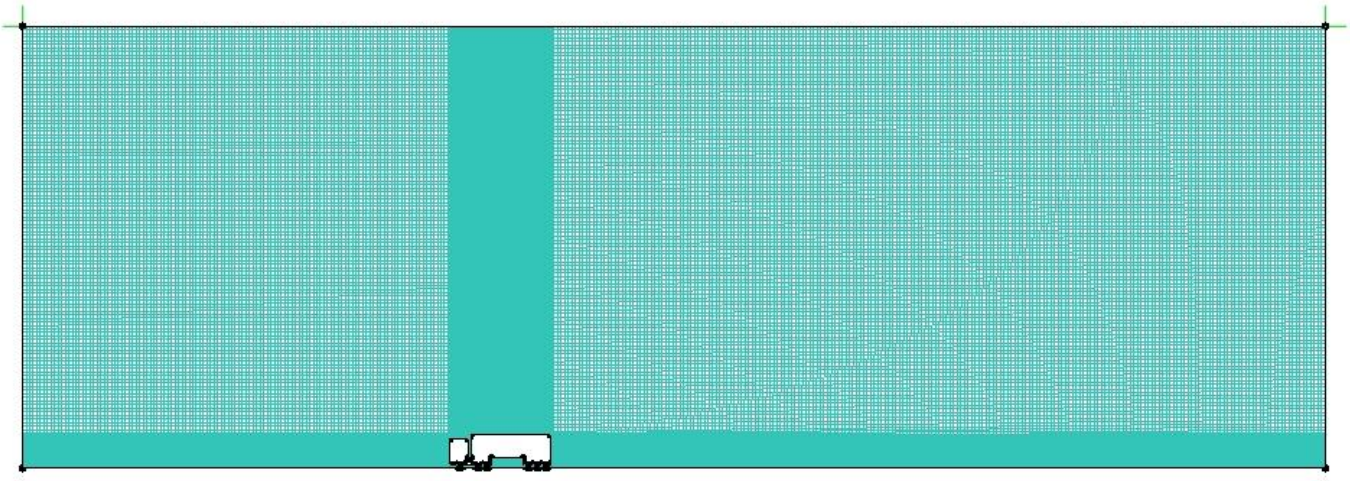

Figure 4.4: Unstructured mesh of full domain.

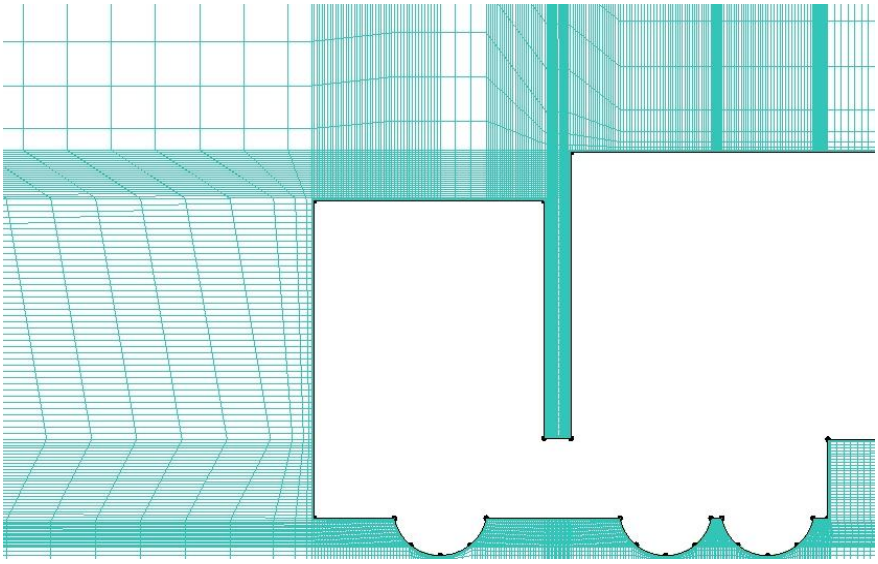

Figure 4.5: Unstructured mesh of lorry front.

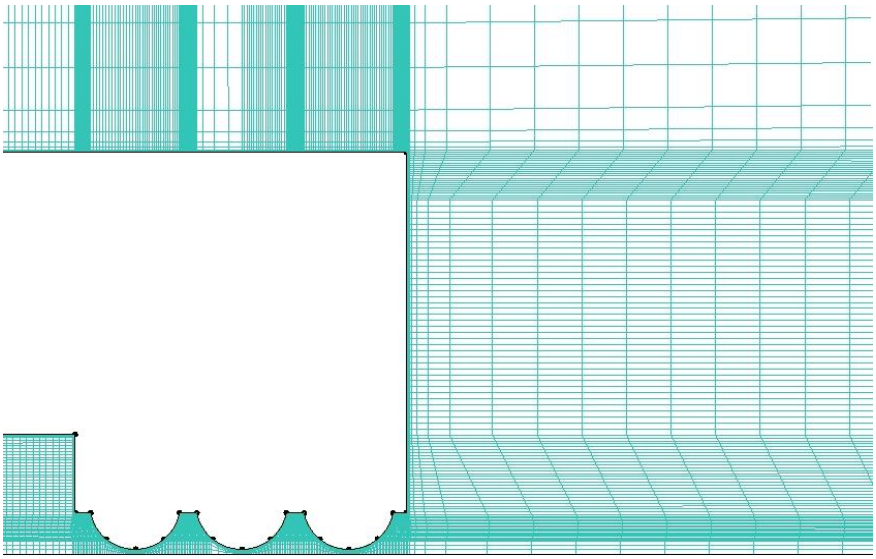

Figure 4.6: Unstructured mesh of lorry rear.

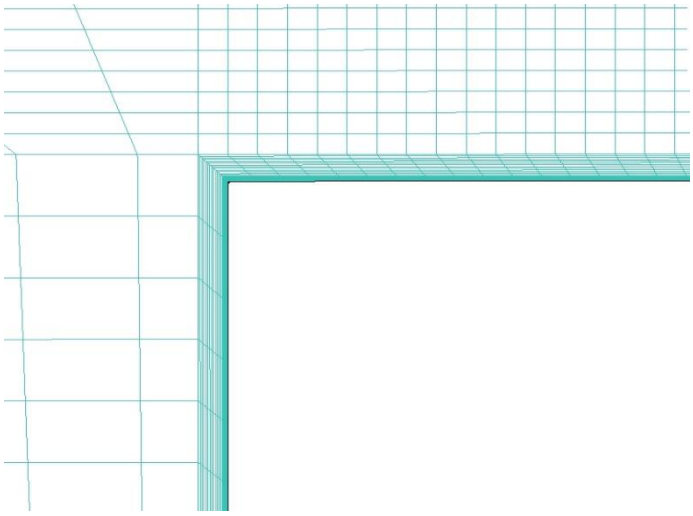

Figure 4.7: Unstructured mesh of lorry near wall.

4.4 ANSYS FLUENT

4.4.1 General Settings

To begin using Fluent, the initial configuration was the setup to enable the mesh to be solved. Firstly, the "Solver", "Velocity Formulation", "Time" and "2D Space" was left at the default settings of "Pressure-Based", "Absolute", "Steady" and "Planar".

The solver was left at pressure-based as the simulation involved incompressible flow and would not have needed density-based which is needed when transonic and supersonic compressible flow are involved (Mangani, Sanz and Darwish, 2016).

Absolute was chosen for the velocity formulation as most of the fluid in the domain was not rotating. The rotating air around the lorry is a small fraction compared to the full domain, therefore if more of the domain had rotating fluid, relative velocity would have been the preferred setting (Sharcnet.ca, n.d.).

The solver for "Time" was the most likely one to change. Steady, short for steady-state, was chosen as it was believed that the mesh would converge and the conditions would become steady over a relatively long time-interval. It was highly dependent on how the shape of the model, therefore the corresponding mesh, as having a more complex shape would likely result in a non-steady-state condition. In simulation, if a more complex model was used alongside a "Steady" time solver then it would have a hard time converging, an oscillatory behaviour in the residual plots would occur and this means that it is a heavy indication of transient behaviour. In the early stages of the study, the more complicated curved shape lorry cab (similar to those shown in figure 2.6) was used, and this lead to converged results only when there was not any trailers attached. However, the flow got complex once the trailers were introduced and the decision to simplify the cab to a simple box geometry was made. The concept of using a transient solver for time is plausible but it is difficult, the need for both physical time steps and the maximum number of coefficient iterations per time step to be set up just is outside the scope (Sharcnet.ca, n.d.).

The simulation involves the full 2D domain of the lorry and the "wind tunnel", therefore it is suitable to choose the "Planar" option in "2D Space" since the other two options of "Axisymmetric" and "Axisymmetric Swirl" is unnecessary and did not apply.

4.4.2 Boundary Conditions

For the boundary conditions, the only setting that was adjusted was in the "inlet". "Components" was selected for the velocity method which split the velocities into the x and y parts. It was assumed that for the y-velocity that it would remain zero and that the air flow from the inlet would meet at a normal to the front face of the lorry. Therefore, for the x-velocity, the chosen speed was based on the dual carriageway speed limit of heavy goods vehicle (HGV) in the UK set by the Highway Code. The limit is from 50mph to 60mph as of 6th April 2015, which the upper limit was taken, and when converted to metres per second was around 27 m/s. The freestream velocity, U_∞ =27 m/s (THE HIGHWAY CODE, 2015).

The initial gauge pressure was set to 101325 Pa which is equivalent to 1 atmospheric pressure at sea-level, which is the altitude most lorries will be cruising at.

For the turbulence settings, it was decided to be left at the default of “Intensity and Viscosity Ratio”. However, looking deeper into the settings, in the “Specification Method”, it was found that there was an option for “K and Omega” which matched the selected turbulence model shown later in section 4.4.3. Using this method would involve the turbulent kinetic energy and specific dissipation rate, both of which is very complicated. There is also the need of analytical description of the boundary layer profile, which isn’t available, so this method won’t be discussed further. The option of “Intensity and Viscosity Ratio” was selected instead, with the corresponding 5% and ratio of 10, respectively. It is said that any value below 1% is considered low, and greater than 10% is high. Therefore, the default value of 5% was a suitable choice as the model doesn’t produce too high or low of turbulence. The same reason for the viscosity ratio, $\frac{\mu_t}{\mu}$, to be left default applies as typically it is set so that $1 < \frac{\mu_t}{\mu} < 10$ (Afs.enea.it, n.d.).

4.4.3 Turbulence Modelling

The selection of the turbulence model was important in this study because it would determine whether the simulation would converge or not. It was decided that the standard k-omega model would be chosen due to how the mesh is formed and the geometry of the lorry.

A few reasons to justify the choice are listed as: The near wall function present around the whole lorry (shown in section 4.3.4), the low Reynolds number model and the definite presence of flow separation. The standard k-omega is the superior choice over the standard k-epsilon and Spalart-Allmaras models when it comes to strong flow separation and strong streamline curves, it is also more robust and accurate for this study (Taştan, 2011).

The comparison between the three have been elaborated in section 2.3.

4.4.4 Reference Values

To make sure the acquired values from the simulation were the correct results, such as the C_D or C_L, the inputted values for all the variables in the reference values needed to be suitable for the base model in this study i.e. the lorry with the box trailer.

There are 10 variables to check in FLUENT: Area (m^2), density (kg/m^3), depth (m), enthalpy (J/kg), length (m), pressure (Pa), temperature (K), velocity (m/s), viscosity (kg/(ms)) and ratio of specific heats.
“Inlet” was selected as where the simulation would compute from as that was the starting region for the domain. There were 7 variables which were kept at the default values assigned by FLUENT: density, enthalpy, pressure, temperature, velocity, viscosity and ratio of specific heat at values of 1.225, 0, 101325, 288.16, 27, 1.789×10^{-5} and 1.4 respectively. These values were either linked from the boundary conditions of the inlet or are the atmospheric sea-level values. The values that needed manual input were the remaining 3. The length and depth (height) of the lorry, as already stated, were 13.8m and 4.52m.

The area was very important in giving the reliable results. The area used was based on the 3D model of the study, which is shown in figure 4.8 below, was the frontal area of the lorry. The width came from the MAN TGX EURO 6 (Automarket.cz, n.d.). This area was based in real scenarios where the air

would be colliding with the lorry face the most. Excluding the side mirror surface area, the total frontal area = 11.3m^2.

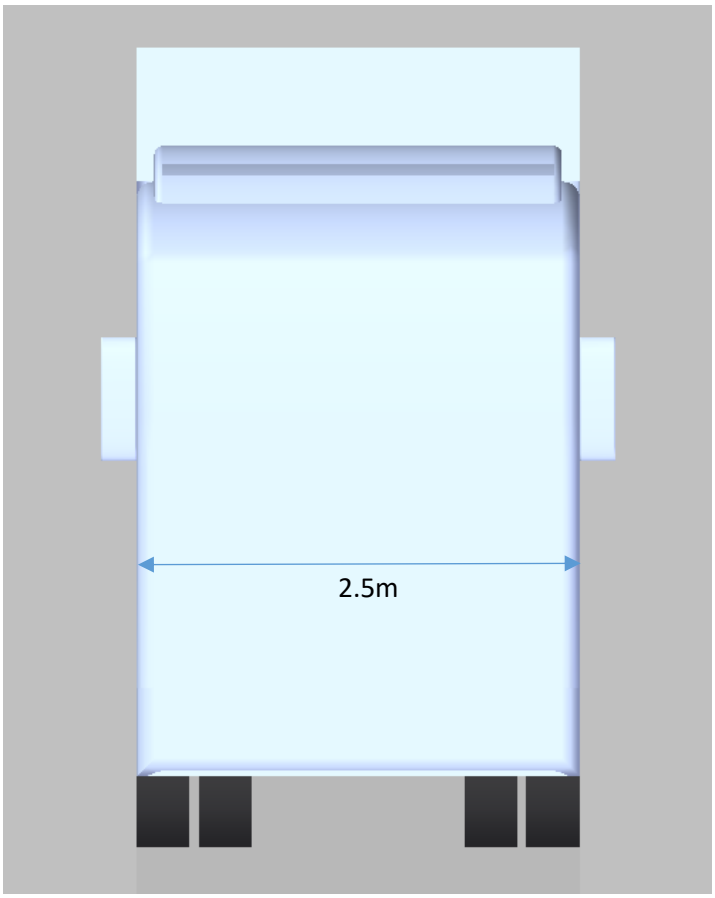

Figure 4.8: Frontal view of lorry.

4.4.5 Solution Methods

4.4.5.1 Numerical Scheme

The scheme chosen for the study was "SIMPLE". For the solver, the whole algorithm consists of 7 main steps:

1) Simulation starts with the initial values
2) Momentum equations are solved until U, V are solved.
3) Calculate coefficients and source terms for the pressure correction
4) Pressure corrections, P'_1 to be solved
5) Calculate the velocity corrections U'_1 and V'_1
6) Update the current P, U and V to the new calculated ones
7) Repeat from step 2 until convergence

For steps 3 and 5, the equations are readily available in other sources, such as T. J. Craft's lecture in "Pressure-Velocity Coupling" (Craft, 2008). Due to the complexity of these equations and how they are typically imbedded into iterative flow solvers, they won't be further mentioned.

4.4.5.2 Spatial Discretization

There were five settings for this section: gradient, pressure, momentum, turbulent kinetic energy and specific dissipation rate.

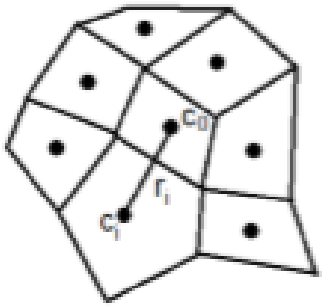

Figure 4.9: Graphical representation of the Least Squared Cell Based gradient method where C_D and C_i are the cell face centres (Cyklis and Młynarczy, 2016).

Firstly, for the gradient there were three options of "Green-Gauss Cell Based", "Green-Gauss Node Based" and "Least Squares Cell Based". The default option of "Least Squares Cell Based" was used as this method is comparable to the other two but is less expensive in terms of simulation time. The solution to this method varies linearly and can been seen in the two cells shown in figure 4.9 (Cyklis and Młynarczy, 2016).

For the other four settings, they were chosen to be second order upwind.

In second order upwind, the values at local nodes are connected by two other upstream values rather than the one (Vanka, 1985) and this means the cell face quantities are computed using a multidimensional linear reconstruction method (Barth & Jespersen, 1989). It has been already been studied by Shyy and Correa for laminar driven cavity problems and other complicated problems, which involve a lot of turbulent flows, that from the results it was concluded that second order upwind is more accurate than the first order upwind scheme (Shyy & Correa, 1986).

4.4.6 Convergence Criteria

For the decision of convergence, during simulation, FLUENT looked at five residuals: continuity, x-velocity, y-velocity, k and omega. After each iteration all the new individual values are compared to the previous ones to produce the left over value, the residue. This residue was then compared with the absolute criteria of 0.001 to see if the value is more or less. If all the values across the 5 residues are less than the criteria, then the calculation was stopped, otherwise the next iteration would occur. It was set so all residue criteria were to be met.
During the testing, the residuals could be monitored via a progress graph as shown as an example below in figure 4.10.

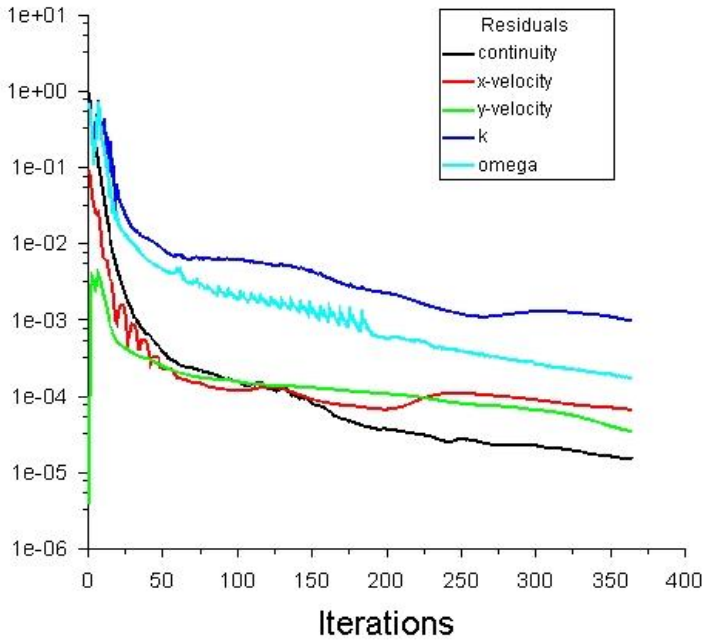

Figure 4.10: Residuals of simulation as iterations increase till convergence (from lorry with box trailer model)..

4.5 Grid Independence Study

The reliability of the mesh is very important in any CFD study. Therefore, before any more of the meshing process was applied to the other three models after doing initial simulations with the base reference model (box trailer), the most optimal nodes setup had to be figured out. This was done with a grid or mesh independence study. To start with, an initial simulation with definite convergence had to be done and this was done with ICEM's default node assignment to each of the body edges. Afterwards, the number of nodes per edge were doubled and another simulation was done to achieve convergence. This process was done a total of three times, meaning the number of nodes per edge by the fourth refinement were greater by 8 fold from the initial node setup.

The most important value to have obtained from each simulation was the drag coefficient which will also reappear in section 5.1 when the comparison between each model is discussed.

Note: After each simulation, the drag coefficient values of each iteration were transferred onto an Excel spreadsheet to find the time-averaged drag coefficient.

Table 1 below shows the C_D of the lorry in simulation at each refinement stage.

Table 1: Drag coefficient values of reference lorry at 4 refinement stages

Total nodes	Refinement	Time-averaged C_D	Error between previous refinement, %
62K	Coarse	1.50	-
90K	Medium	1.76	17.6
186K	Fine	1.85	4.9
266K	Really fine	1.96	6.0

As highlighted in green, it was best to use a fine mesh in the simulation due to it having the lowest error compared to the other refinements. Coarse-medium error is too big at 17.6%, fine-really fine error is at 6.0% which is acceptable but for a mesh between medium and fine refinement at 4.9% it was the most accurate and reliable setup to be carried forward for the remaining models.

5. Results and Discussion

5.1 Comparison of Time Averaged Coefficient of Drag and Lift

Table 2: Time averaged coefficient of drag and lift for each model overall

Model	C_D	C_L	ΔC_D	ΔC_L
1. Base reference model (box trailer)	1.85	-1.01	-	-
2. Curved trailer	1.72	-1.35	-0.13	-0.34
3. Boat tail ended curved trailer	1.73	-1.17	-0.12	-0.16
4. Spoiler ended curved trailer	1.90	-1.14	+0.05	-0.13

The key part to investigate the efficiency reduction is to observe the drag and lift coefficient changes between all the models. As shown above in table 2, the fourth and fifth columns show the changes of C_D and C_L in relation with the reference model.
For each value of C_D and C_L, it was taken as a time averaged value, this was done by outputting the raw data containing the results per iteration onto Excel and using the average function to calculate it. The start of the range of values taken for the average was chosen when the fluctuation of the C_D and C_L graphs started to stabilise.

Note: the coefficient of drag and lift values are for the overall lorry. ANSYS Fluent takes the average across the whole model at the instantaneous time during the simulation iteration.

For example, marked below in red in figure 5.1, the start value was around 35 iterations and so in Excel the drag and lift coefficient values were selected at that point and used for the start of the average.

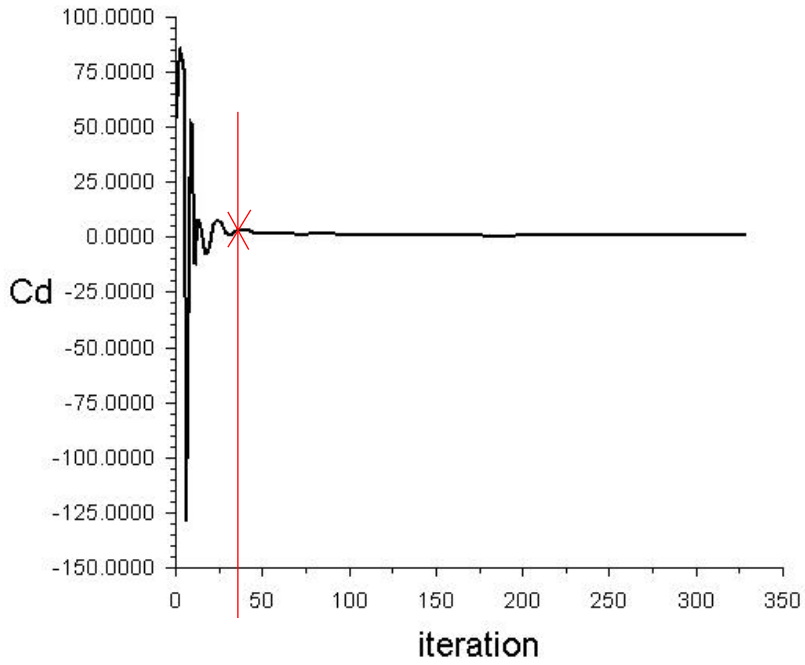

Figure 5.1: Plot of Cd over 329 iterations, red line marks start of stability (from box trailer simulation).

Out of the two coefficients, the drag is considered more important in this study as the factors involved, contributing to the efficiency, outweigh those produced by the lift coefficient. However, it was still valid to look at C_L to compare the changes and see if the changes are drastic which as shown in table 2, did have a slight impact compared to the reference model.

Coefficient of lift

Firstly, the coefficient of lift will be discussed and how lift is involved in vehicles that aren't airborne, such as aircrafts. From other studies' investigations it has been shown that the lower the lift is in a vehicle, the more beneficial it is in terms of aerodynamic and stability performances. By having a negative lift at the rear axle, it would increase the stability margin and allow for better vehicle control under all driving conditions. Therefore, it is best for a negative lift or at least zero, if it is positive then there would be negative effects. Another benefit of lowering the lift coefficient is that it would increase the maximum lateral acceleration potential and greatly improve the handling. This is especially crucial in smaller vehicles such as race cars (Scibor-Rylski and Sykes, 1984; Assmann and Witte, 1982; Ahmed and Hucho, 1998).

Looking at the results, it can be seen that the lorry with the curved trailer produced the least amount of lift overall. The 3rd and 4th models produced almost double the amount of lift compared to the 2nd which means the curved trailer would be the best for handling. Although the boat-tail and the spoiler models have only a 0.03 difference in C_L, the difference in their coefficient of drag, which will be discussed next, puts a definite winner between the two.

Coefficient of drag

When the coefficient of drag of the models are compared, it can be seen that the curved trailer once again is better than the other two models. Although the difference between it and the 3rd trailer is 0.01, the C_L in the curved trailer, as discussed before, is more than double smaller compared to the other two models which justifies it to be the best out of the models.

The drag of the boat tail model would have been at the lowest drag configuration due to its' optimal slant angle of 12.5°. However, this drag was still slightly higher than the curved trailer which the slant angle was set at 7.8° and not at the optimal angle (the curved trailer slant angle was not taken into proper consideration when the model was created). Looking at equation 1, the reason to the higher C_D in the boat tail model might be due to the decrease in the stream velocity behind the trailer as the other constants, surface area increases and density would be constant.

Although the slant angle of the curved trailer was not set to 12.5°, it can be seen from figure 2.2, that the difference in the coefficient of drag between 7.8° and 12.5° is so small that it can be negligible.

Comparing the spoiler model to the reference model, it has a small increase in drag but due to its decrease in lift, it can be said that the benefits of the vehicle handling can make the +0.05 C_D overlooked.

The overall increase in efficiency for the coefficient of drag in the best model, the curved trailer, compared to the base model was 7.0% and for the coefficient of lift was 33.7%.

5.2 Velocity Contours

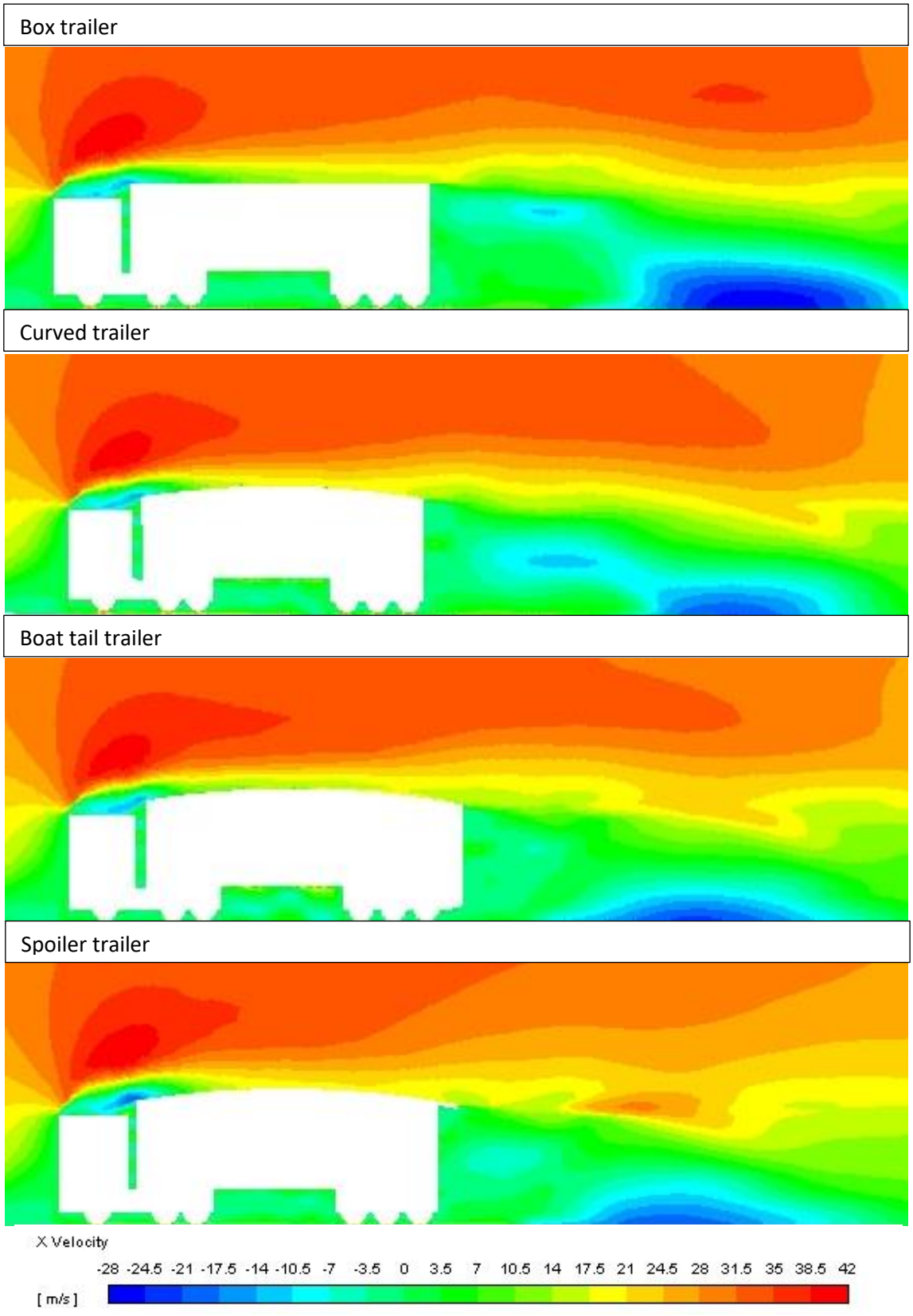

Figure 5.2: X-velocity contours of all the models.

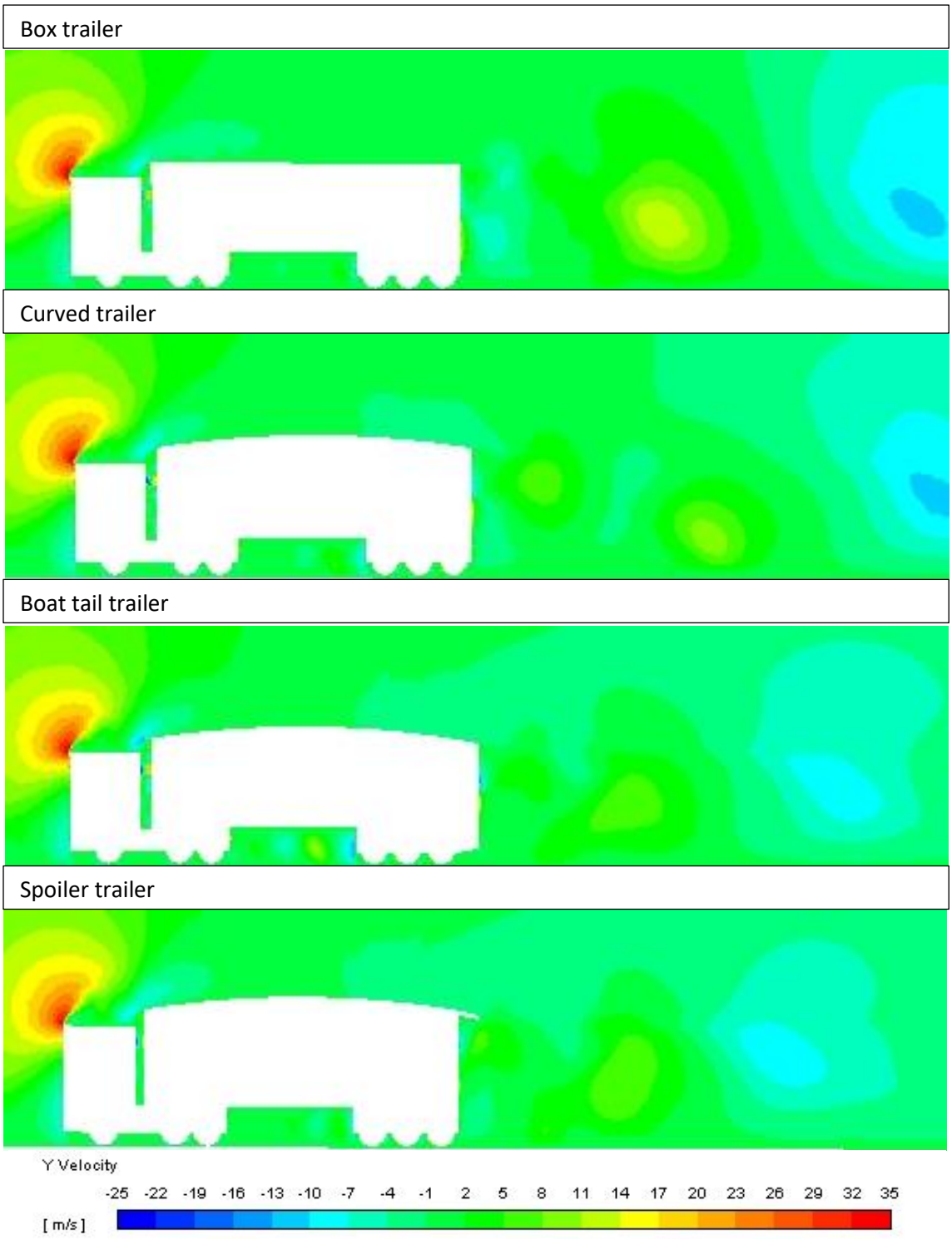

Figure 5.3: Y-velocity contours of all the models.

Velocity contours are a general way to visualise the simulation and the selected parameter of interest. In the case of figures 5.2 and 5.3, the x and y-velocities were selected as they would show the whereabouts of the vortices. The positive flow is towards the right side for x and upwards for y.

In this study's case, the wake region is more relevant to the reduction in drag to improve the efficiency, due to the drag reduction devices being implemented to the trailer and not on the cabin. The flow

separation region at the leading edge of the cabin top would be similar for all the models because of the cabins being the same shape. Another point to note is that since it is only a 2D simulation, a small gap of 5 cm was left between the ground and the wheels. This was so that during simulation, the air flow can travel through the bottom side of the lorry, and out through the rear side. This has to be done otherwise the information of the flow cannot be transmitted to the underside of the lorry, whereas in a 3D model, flow could just go through the gap between the left and right wheels. This was the reason, as shown in figure 5.4 below, that there was a high velocity region right underneath the wheel where the flow accelerates due to the pressure drop. It is also the reason the flow velocity in front of the lorry face does not appear uniform coming towards it, as some of the flow gets reflected from the wheels and counters the incoming flow, causing the velocity to slow down before it comes close to the lorry front (Shown in figure 5.5).

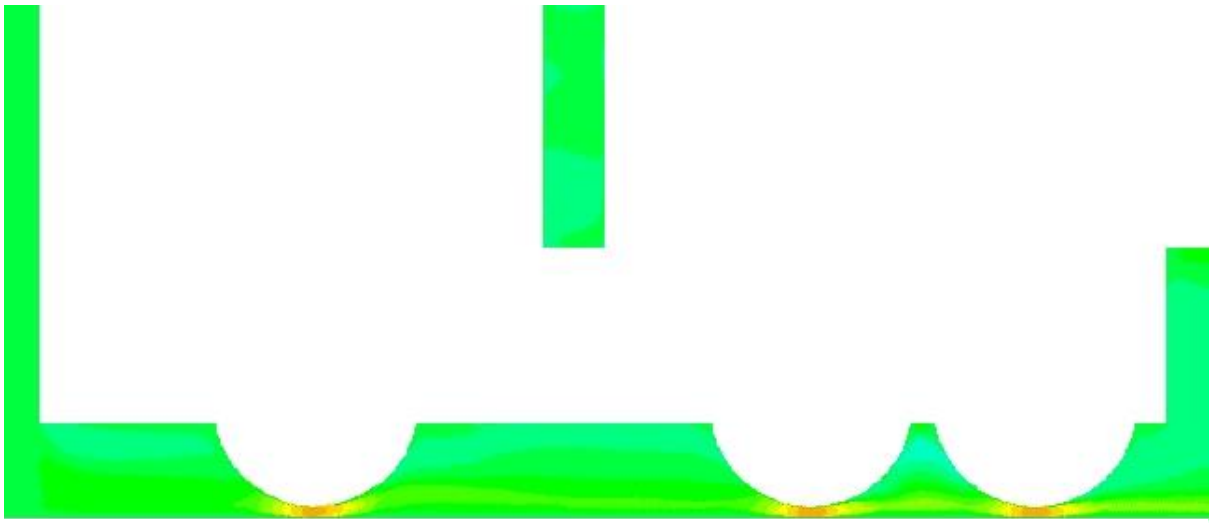

Figure 5.4: Close up view of velocity contour at the wheels region (based from reference model).

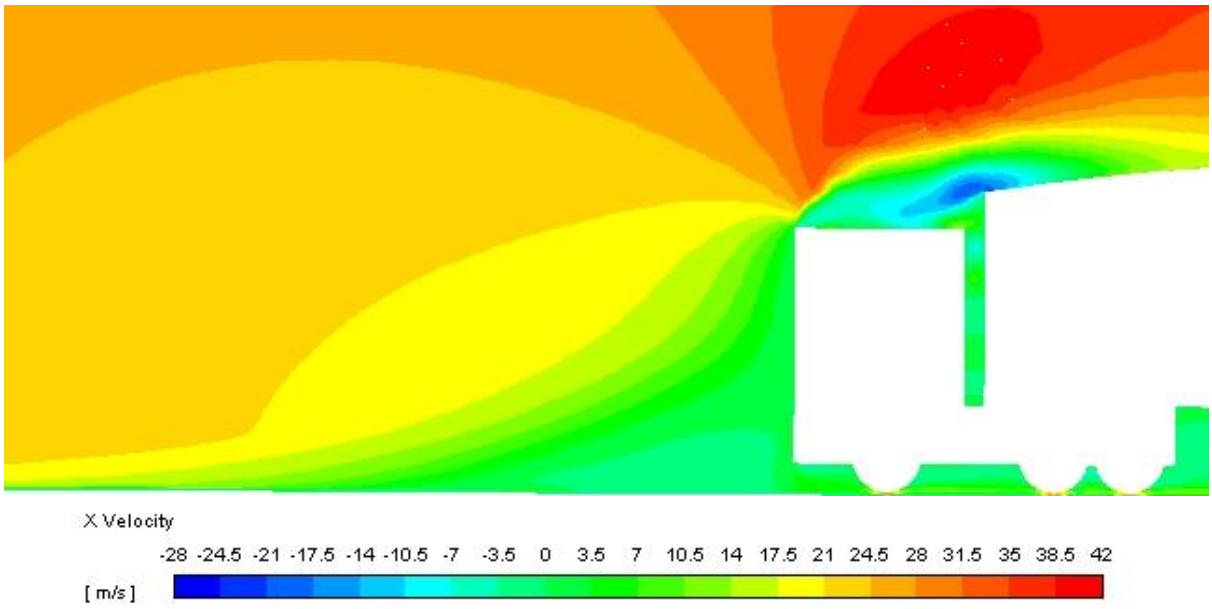

Figure 5.5: Flow region in front of lorry cabin.

To start with, at the front side of the lorry, the obvious presence of the leading edge separation can be spotted by the red region above the cabin top. This was followed by an almost immediate recirculation bubble between the cabins and their trailers which caused the flow above it to accelerate back towards the top surface of the trailers. In the box and boat tail trailers, this flow travels at a speed of around 15 m/s and only reaches 20 m/s when near the end of the length of the trailer, whereas the other 2 models' flows reached 20 m/s right from half way across the trailer.

For each model the flow separates again at the trailing edge of the trailers, this is indicated by the drop of velocity where the wake region is. There is a clear vortex region (the large blue area) where the reverse flow of each model is most prominent, with the box trailer having the largest region, followed by the boat tail and spoiler models, with the curved trailer having the least reverse flow. In figure 5.3, there is more variance in y-velocity for the box trailer, which also justifies it having the strongest vortexes.

Comparing another studies' velocity contours in figure 5.6 (Lo and Kontis, 2017), it can be seen that their vortex region appears right behind the trailer, which is not present in this study case. The main difference is that in 3D simulation, there is more flow coming from under the lorry which generates the lower shear layer. This force coils upwards and interacts with the upper shear layer, causing a vortex to form. In 2D flow, there is almost no lower shear layer, the small amounts that are present are coming from the small gap between the wheels and the ground, and this meant that the upper shear layer generated the vortexes further downstream. It can be seen in figure 5.7, circled in red, that there is a weak reverse flow near the backside of the trailer at the bottom where some of the lower shear layer coil up. However, it does not reach far or high enough to affect the upper shear layer. The vortex circled in blue would be the solo work of just the upper shear layer. The similarity between the two works is that the stagnation points in the flow field are located in the same area.

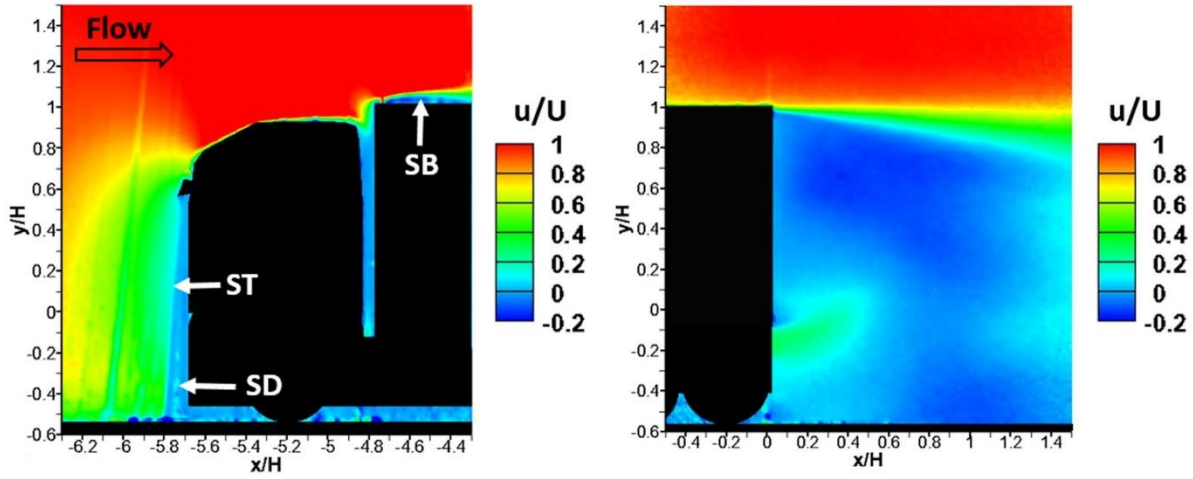

Figure 5.6: Velocity contours over the front and rear parts of an articulated lorry model with normalised velocity in x-direction (Lo and Kontis, 2017).

As already stated, the flow acts considerably more different in 3D due to the limitations of where the flow can access. In 3D, the possibility of the flow in the Z axis is available which means a lot more complexion and would require a deeper knowledge in the field. For future research, it would be best to look into different kinds of contours such as the turbulence and the pressure, and if possible the 3D simulation. This would allow for multiple perspectives of the models for analysing. In the next section,

the velocity profiles which are a more numeric approach to determining the flow changes on the lorry, will be analysed.

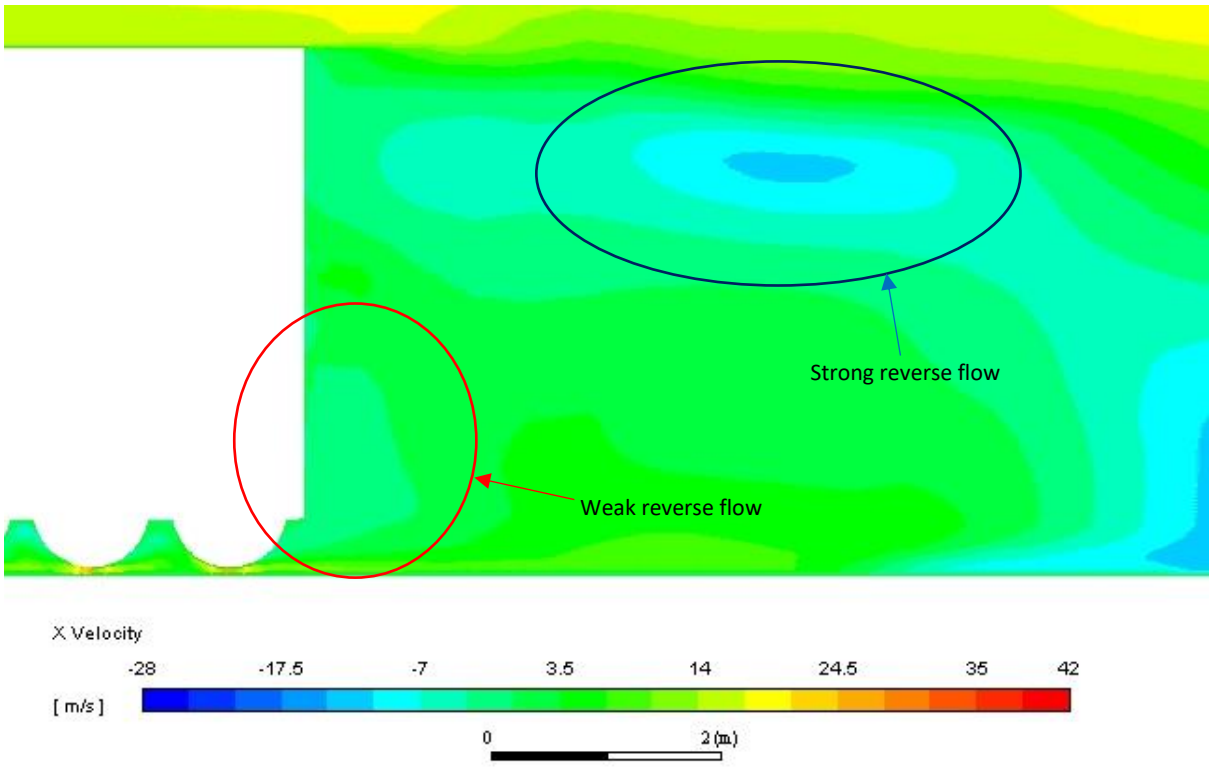

Figure 5.7: X-velocity contour of flow near the backside of the trailer.

5.3 Wake region

Generating the graphs for the wake regions was key to comparing how the velocities and vorticities are affected over the distance behind the trailer for each individual model. It was decided that for each model there would be a total of 6 wake sections and each would span a distance of 5 metres. By using ANSYS FLUENT's functions, it was possible to output the data to be able to create the velocity profiles in EXCEL, section 5.3.1 will show the velocity profiles for the X-velocity (U), Y-velocity (V) and Vorticity magnitude (Ω) of all the models. To compare between models, it was best to set the y-axis to dimensionless by finding the ratio of the trailer height to the base model trailer reference height of 4.1 metres.

Below is a diagram showing how the wake region is broken down and where the starting point of x=0 metres is relative to in this section.

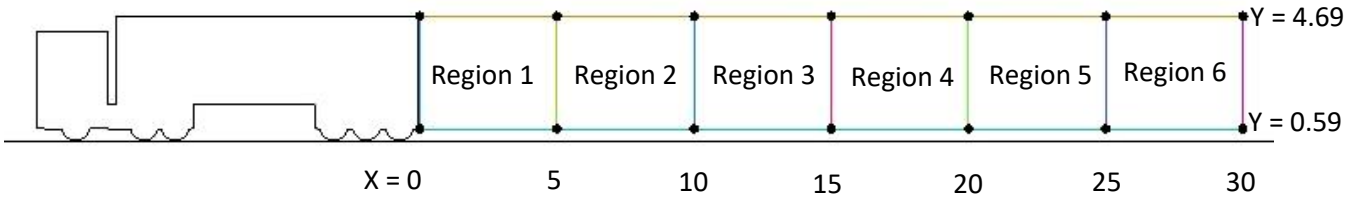

Figure 5.8: Wake region breakdown behind the trailers of the models at 5 metre intervals.

Shown below in figures 5.9 to 5.11, the lower limit and upper limit of the normalised y-locations were 0.144 and 1.14 respectively. The normalised y-location, y/H, was done to be able to compare how the wake changes across the regions as the flow comes off the back of the trailer for each model.

5.3.1 Velocity profiles: X, Y & Ω

At first glance, it can be seen that the general trend for all the models are similar for each region, however each have their own variation. It shall be discussed further about the significant meaning of the changes.

From the first wake region in figure 5.9, it can be seen that the box trailer has the highest minimum x-velocity out of the models, at a value of around U = -12 m/s in the normalised y-location y/H = 0.90. The other 3 models' lowest peaks lie between 0.60 < y/H < 0.70 and the minimum x-velocity of the curved and spoiler trailers are nearly the same at U = -5 m/s, whereas the boat tail model had the lowest of U = -3 m/s.

In the second region (5 to metres behind the trailer back), the lowest peak x-velocity for the box trailer increases to U = -0.5 m/s but falls to y/H = 0.54. Whereas, for the curved trailer and boat tail models the minimum x-velocity drops U = -10 and -7.5 m/s, respectively. The boat tail remains the same magnitude, but along with the spoiler trailer, the normalised y-location drops to the bottom. Judging between both regions 1 and 2, it seems that the box trailer showed traits of initial high y location reverse flow but the reverse flow got slightly weaker as it descends down to y/H = 0.54. The upper shear layer is dissipated downwards. The reverse flow for the curved and boat tail trailers gets stronger as it goes from 0 to 10 metres and heads towards the ground. Looking at the y-velocity (figure 5.10), it can be seen that although in the x-velocity the box trailer the reverse flow gets weaker, the magnitude of the y-velocity from region 1 to 2 increases from V = -5 m/s to V = 12.5 m/s, this suggests that the overall vortex gets stronger.

For the 3rd until 4th regions (10 – 15 m), the reverse flow in the lower normalised y-locations which are around y/H < 0.54 are now much stronger, with each of them having U < -15 m/s. This corresponds to the big reverse flow region near the ground in the velocity contour from figure 5.2. As the flow moves to the 4th region, the reverse flow for the boat tail and spoiler models start getting weaker whereas the other 2 are still strong. When observing the y-velocity, the trend of the flow is similar, with the box and curved trailer having a sustained strong reverse flow. Overall, at this point the flow in the boat tail and curved models started to return to a uniform flow.

For the last two regions, it can be clearly seen that the flow is less disruptive and more uniform and is an indication that the flow is returning to a uniform free stream flow. It would still take a long distance to reach the free stream velocity behind the wake region but eventually it will return to U =27 m/s.

Graphs of the vorticity magnitude (figure 5.11) were also plotted and enables the ability to accurately pin-point the locations of the specific shear layers present. Due to the simulation being in 2D, the only shear layer contribution is from the upper shear layer. On the graph it is represented by the big peak which appears to be a sudden spike. Each peak in vorticity magnitude links in to the x and y-velocity of the flow, as the vorticity is proportionate to the differential product of the two.

To conclude, the base model would produce the most drag due to the big presence of the vortexes. The drop in pressure in the box trailer model was the greatest and therefore would cause a lot of drag due to the front of the lorry having a much higher pressure. However, compared to the coefficient of drag results, the curved trailer showed more reverse flow than the boat tail and the spoiler models. It is hard for a final judgement to decide the most efficient model in this study from what has been done due to the lack of experimental results.

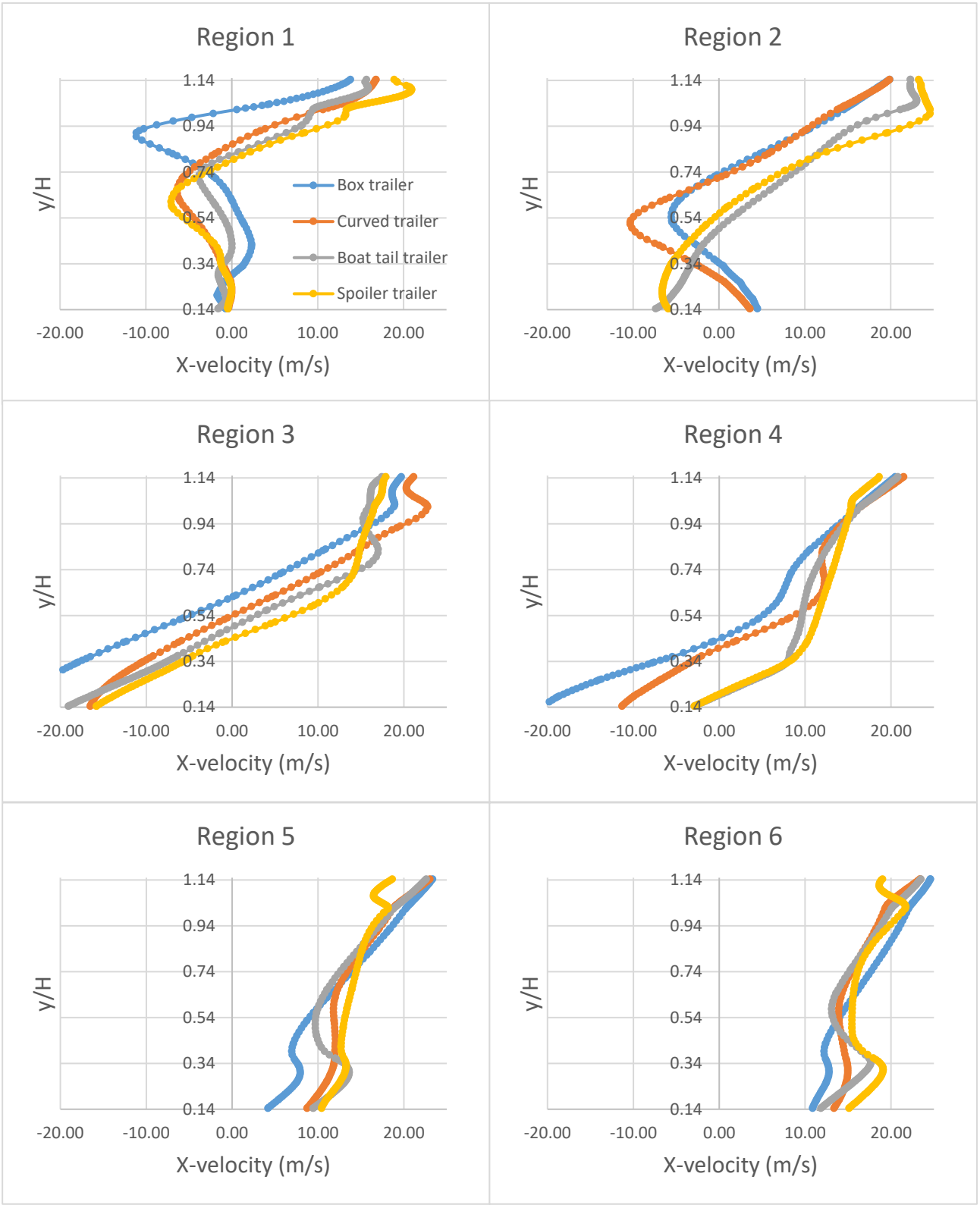

Figure 5.9: Graphs to show the change of x-velocity over y/H for all the models across a span of 30 metres.

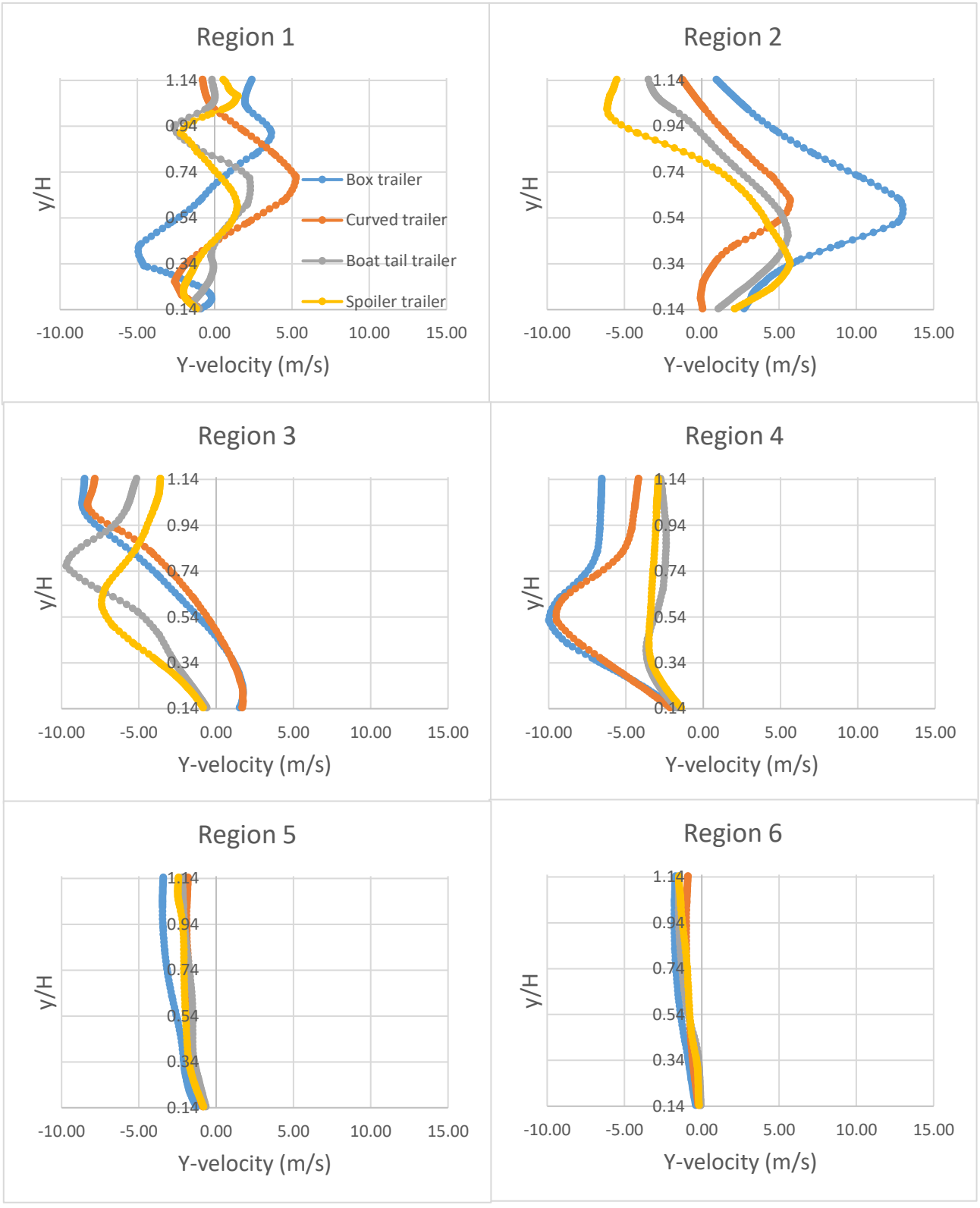

Figure 5.10: Graphs to show the change of y-velocity over y/H for all the models across a span of 30 metres.

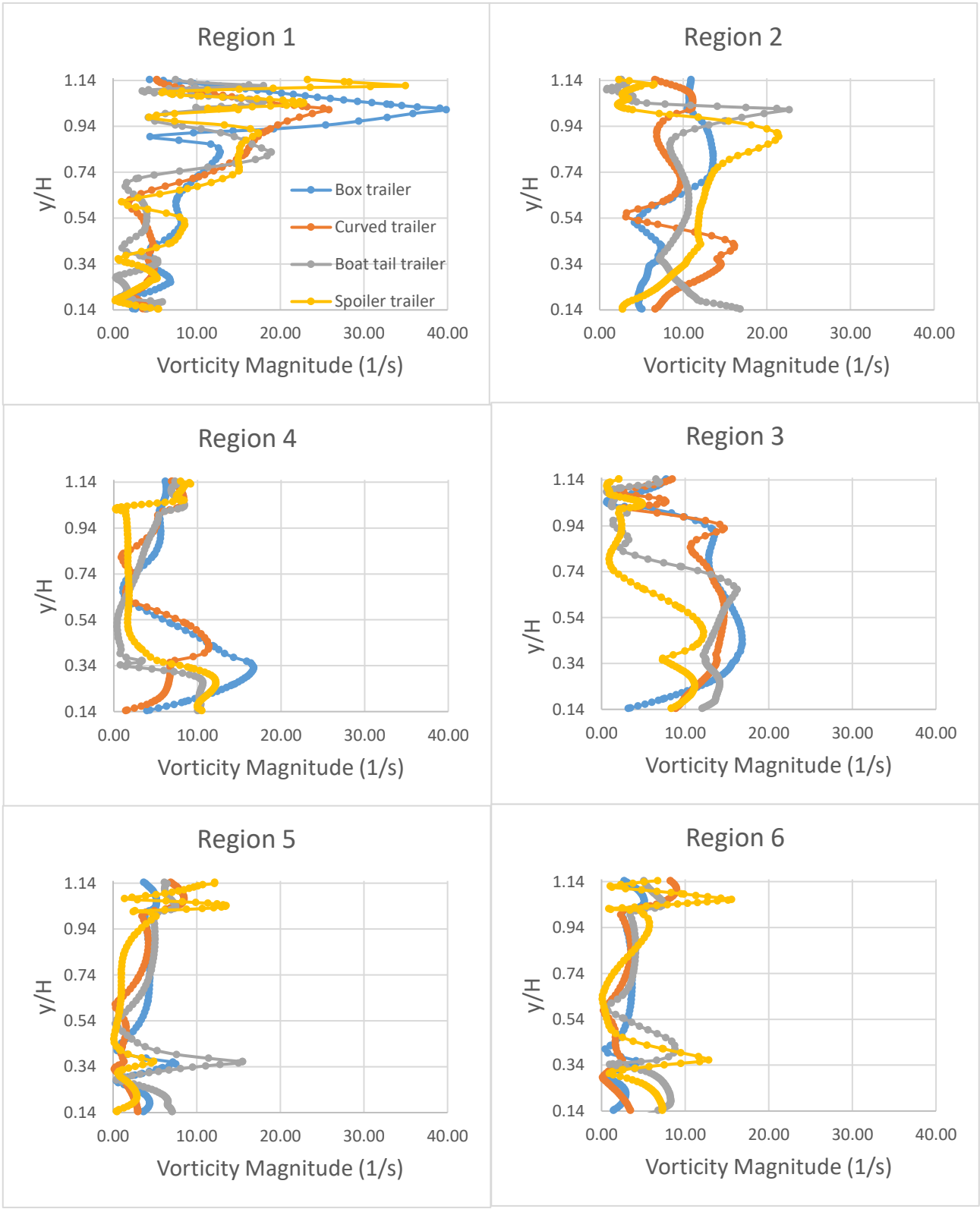

Figure 5.11: Graphs to show the change of vorticity magnitude over y/H for all the models across a span of 30 metres.

6. Conclusion

To conclude this study, it can be seen that by adding drag reduction devices to the base model, the flow around the lorry can be changed quite drastically. Although the effect of 2D flows vary quite differently compared to 3D, the results generated from looking at the coefficient of drag and lift, velocity contours and profiles, can most certainly be a stepping stone for the selection of a more efficient model. It was found that the best efficiency increase in C_D was 7.0% and in C_L was 33.7% and was achieved by the lorry with the top surface curved trailer. From the velocity profiles, it was shown that the vortexes formed from the boat tail and spoiler trailer models were not as strong as their competitor models. This resulted in a lower drag and better performance in those two models.

7. Future Recommended Work

There are many ways to improve this study to fit a real life application. Firstly, if this study was to be redone, the first most important step would be operating everything in three-dimension. In reality, the flow going around the side of the lorry would indefinitely change the whole flow region. It also allows for the concept of crosswind to be applied, which would shift more focus onto the lift of the overall lorry as handling would become a big factor in ensuring safety for the driver.

Leading off from this, the choice of CFD programmes to be used next time can be better suited for managing 3D modelling. For example, ANSYS CFX or SimScale. By having a 3D model, it allows for a 3D printed model to be made and wind tunnel testing to be conducted which would show more reliability in the models and capture any environment conditions which computer simulations might not be able to recreate.

Secondly, more drag devices should be investigated which include the side extenders, cab deflector or an undercarriage straight skirt, as mentioned before. These would give more variety to the study and show more realism.

Next, the general setup of the other parts of the lorry, besides the trailer, and parameters should be explored. There are a few options for adjusting the geometry but the main ones are the shape of the cabin and the gap between the trailer and the cabin. The freestream velocity should also be adjusted to have a bigger range to see how the lorries are affected at low and high speeds.

Finally, as the future is coming and technology would advance, it would be perfect to start having more innovative and unique designs. It may be best to create an idea from scratch, with justified reasons, and test it in these CFD simulations. For the last point for improvement, in later studies, future-proof technology shall be investigated and potentially can supply the world with eco-friendly heavy vehicles.

References

Afs.enea.it. (n.d.). *ANSYS FLUENT 12.0 User's Guide - 7.3.2 Using Flow Boundary Conditions*. [online] Available at: http://www.afs.enea.it/project/neptunius/docs/fluent/html/ug/node238.htm [Accessed 29 Apr. 2019].

Ahmed, S. and Hucho, W. (1998). *Aerodynamics of road vehicles*. 4th ed. Warrendale, Pa.: Society of automotive engineers, pp.60, 62, 71-73, 386, 426-427.

Ahmed, S., Ramm, G. and Faltin, G. (1984). Some Salient Features Of The Time-Averaged Ground Vehicle Wake. *SAE Technical Paper Series*.

ANSYS Inc. (2006). *Modeling Turbulent Flows*.

Ali, Z., Tucker, P. and Shahpar, S. (2016). *Optimal Mesh Topology Generation for CFD*. [online] p.2. Available at: https://www.repository.cam.ac.uk/handle/1810/262813 [Accessed 27 Apr. 2019].

Assmann, W. and Witte, L. (1982). Einfluß der Aerodynamik auf das Fahrverhalten eines Pkw. In: *Vehicle Aerodynamics Symposium*. Wolfsburg.

Automarket.cz. (n.d.). *MAN TGX 18.440 BLS EURO 6 4x2 - standard - Automarket*. [online] Available at: https://www.automarket.cz/en/man-tgx-18-440-bls-euro-6-4x2-6101 [Accessed 1 May 2019].

Axerio-Cilies, J. (2012). *Predicting Formula 1 tire aerodynamics: sensitivities, uncertainties & optimization.* PhD. Stanford.

Balkanyi, S., Bernal, L. and Khalighi, B. (2002). Analysis of the Near Wake of Bluff Bodies in Ground Proximity. *Fluids Engineering*.

Barth, T. and Jespersen, D. (1989). *The design and application of upwind schemes on unstructured meshes*. Moffett Field.

Beardmore, R. (2013). *Flow separation on streamlined and bluff bodies*. [image] Available at: http://www.roymech.co.uk/Related/Fluids/Fluids_Drag.html [Accessed 12 May 2019].

Bearman, P., De Beer, D., Hamidy, E. and Harvey, J. (1988). The Effect of a Moving Floor on Wind-Tunnel Simulation of Road Vehicles. *SAE Technical Paper Series*.

Buil, R. and Ferrer, L. (2009). Aerodynamic Analysis of a Vehicle Tanker. *Journal of Fluids Engineering*, [online] 131(4), p.041204. Available at: http://fluidsengineering.asmedigitalcollection.asme.org/article.aspx?articleid=1433587 [Accessed 13 May 2019].

Castellucci, P. and Salari, K. (2005). Computational Simulation of Tractor-Trailer Gap Flow with Drag-Reducing Aerodynamic Devices. *SAE Technical Paper Series*. [online] Available at: https://saemobilus.sae.org/content/2005-01-3625/ [Accessed 30 Apr. 2019].

Choi, H., Lee, J. and Park, H. (2014). Aerodynamics of Heavy Vehicles. *Annual Review of Fluid Mechanics*, [online] 46(1), p.460. Available at: https://www.annualreviews.org/doi/pdf/10.1146/annurev-fluid-011212-140616 [Accessed 30 Apr. 2019].

Cooper, K. (2003). Truck Aerodynamics Reborn - Lessons from the Past. *SAE Transactions*, [online] 112, pp.132-142. Available at: https://www.jstor.org/stable/44718756?seq=1#page_scan_tab_contents [Accessed 13 May 2019].

Cooper, K. and Leuschen, J. (2005). Model and Full-Scale Wind Tunnel Tests of Second-Generation Aerodynamic Fuel Saving Devices for Tractor-Trailers. *SAE Technical Paper Series*. [online] Available at: https://saemobilus.sae.org/content/2005-01-3512 [Accessed 13 May 2019].

Cooperativeenergy.coop. (2016). *When will fossil fuels run out? | Co-operative Energy*. [online] Available at: https://www.cooperativeenergy.coop/customer-service/frequently-asked-questions/green-energy/green-energy-faqs/when-will-fossil-fuels-run-out/ [Accessed 19 Apr. 2019].

Craft, T. (2008). *Pressure-Velocity Coupling*. Available at: http://cfd.mace.manchester.ac.uk/twiki/pub/Main/TimCraftNotes_All_Access/ms4-pressvel.pdf [Accessed 11 May. 2019]

Cyklis, P. and Młynarczy, P. (2016). *The influence of the spatial discretization methods on the nozzle impulse flow simulation results*. [online] Elsevier Ltd., p.399. Available at: https://core.ac.uk/download/pdf/82268909.pdf [Accessed 1 May 2019].

Englar, R. (2001). Advanced Aerodynamic Devices to Improve the Performance, Economics, Handling and Safety of Heavy Vehicles. *SAE Technical Paper Series*. [online] Available at: https://www.sae.org/publications/technical-papers/content/2001-01-2072/ [Accessed 13 May 2019].

FLUENT Inc. (2003). *FLUENT 6.1 User's Guide*. Lebanon: FLUENT Inc., pp.659-664.

Gilliéron, P. and Kourta, A. (2009). Aerodynamic drag reduction by vertical splitter plates. *Experiments in Fluids*, [online] 48(1), pp.1-16. Available at: https://link.springer.com/article/10.1007/s00348-009-0705-7 [Accessed 13 May 2019].

Haff, J., Jönsson, M., Richard, H. and Loose, S. (2009). Experimental investigation on a detailed European tractor-trailer configuration. In: *Euromech Colloquium 509 "Vehicle Aerodynamics"*. Berlin, pp.104-115.

Han, T., Sumantran, V., Harris, C., Kuzmanov, T., Huebler, M. and Zak, T. (1996). Flow-Field Simulations of Three Simplified Vehicle Shapes and Comparisons with Experimental Measurements. *SAE Technical Paper Series*.

Howell, J., Sheppard, A. and Blakemore, A. (2003). Aerodynamic Drag Reduction for a Simple Bluff Body Using Base Bleed. *SAE Transactions*, [online] 112, pp.1085-1091. Available at: https://www.jstor.org/stable/44745484?seq=1#page_scan_tab_contents [Accessed 13 May 2019].

Hucho, W. and Sovran, G. (1993). *Aerodynamics of Road Vehicles*. [online] Michigan. Available at: https://www.annualreviews.org/doi/pdf/10.1146/annurev.fl.25.010193.002413 [Accessed 11 May 2019].

Hyams, D., Sreenivas, K., Pankajakshan, R., Stephen Nichols, D., Roger Briley, W. and Whitfield, D. (2011). Computational simulation of model and full scale Class 8 trucks with drag reduction devices. *Computers & Fluids*, [online] 41(1), pp.27-40. Available at: https://www.sciencedirect.com/science/article/pii/S0045793010002434 [Accessed 13 May 2019].

Khalighi, B., Zhang, S., Koromilas, C., Balkanyi, S., Bernal, L., Iaccarino, G. and Moin, P. (2001). Experimental and Computational Study of Unsteady Wake Flow Behind a Bluff Body with a Drag Reduction Device. *SAE Transactions*, [online] 110, pp.1209-1222. Available at: https://www.jstor.org/stable/44730974?seq=1#page_scan_tab_contents [Accessed 13 May 2019].

Kim, J., Lee, S., Kim, M., You, D. and Lee, S. (2015). *Schematic and perspective of (a) 2D cab-roof fairing (CRF) based on the streamlined curvature, (b) 2D CRF with rounded edges (3D CRF), and (c) the modified CRF*. [image] Available at:

https://www.researchgate.net/publication/313941703_Salient_drag_reduction_of_a_heavy_vehicle_using_modified_cab-roof_fairings [Accessed 13 May 2019].

Leuschen, J. and Cooper, K. (2009). Summary of Full-Scale Wind Tunnel Tests of Aerodynamic Drag-Reducing Devices for Tractor-Trailers. [online] pp.451-462. Available at: https://link.springer.com/chapter/10.1007%2F978-3-540-85070-0_41 [Accessed 13 May 2019].

Littlewood, R. and Passmore, M. (2012). Aerodynamic drag reduction of a simplified squareback vehicle using steady blowing. *Experiments in Fluids*, [online] 53(2), pp.519-529. Available at: https://link.springer.com/article/10.1007/s00348-012-1306-4 [Accessed 13 May 2019].

Lo, K. and Kontis, K. (2017). Flow around an articulated lorry model. *Experimental Thermal and Fluid Science*, 82, pp.58-74.

Malviya, V., Mishra, R. and Fieldhouse, J. (2009). CFD Investigation of a Novel Fuel-Saving Device for Articulated Tractor-Trailer Combinations. *Engineering Applications of Computational Fluid Mechanics*, [online] 3(4), pp.587-607. Available at: https://www.tandfonline.com/doi/abs/10.1080/19942060.2009.11015293 [Accessed 13 May 2019].

Mangani, L., Sanz, W. and Darwish, M. (2016). *Comparing the performance and accuracy of a pressure based and density-based coupled solver*. [online] Available at: https://hal.archives-ouvertes.fr/hal-01894391/document [Accessed 28 Apr. 2019].

McCallen, R., Salari, K., Ortega, J., Castellucci, P. and Eastwood, C. (2005). *DOE project on heavy vehicle aerodynamic drag FY 2005 annual report*. Livermore, CA.

McNamara, K. (2015). *After flow wake*. [image] Available at: https://arc.aiaa.org/doi/abs/10.2514/6.2018-3964 [Accessed 12 May 2019].

Minguez, M., Pasquetti, R. and Serre, E. (2008). High-order large-eddy simulation of flow over the "Ahmed body" car model. *Physics of Fluids*, [online] 20(9), p.095101. Available at: https://aip.scitation.org/doi/pdf/10.1063/1.2952595?class=pdf [Accessed 11 May 2019].

Ortega, J. and Salari, K. (2004). An Experimental Study of Drag Reduction Devices for a Trailer Underbody and Base. *34th AIAA Fluid Dynamics Conference and Exhibit*. [online] Available at: https://arc.aiaa.org/doi/10.2514/6.2004-2252 [Accessed 13 May 2019].

Peterson, R. (1981). *Drag Reduction Obtained by the Addition of a Boattail to a Box Shaped Vehicle*. MSc. California Polytechnic State University.

Puiu, T. (2018). *How long before the world runs out of fossil fuels?*. [online] ZME Science. Available at: https://www.zmescience.com/other/feature-post/how-long-fossil-fuels-last-43432/ [Accessed 19 Apr. 2019].

Raemdonck, G. and Tooren, M. (2009). *A practical scientific approach for aerodynamic truck design.* pp.293-303.

Rodríguez, S. (2014). *Turbulence Modeling Tips*.

Scibor-Rylski, A. and Sykes, D. (1984). *Road vehicle aerodynamics*. 2nd ed. London: Pentech.

Sharcnet.ca. (n.d.). *1.2.1. Steady State and Transient Flows*. [online] Available at: https://www.sharcnet.ca/Software/Ansys/16.2.3/en-us/help/cfx_mod/i1298451.html [Accessed 28 Apr. 2019].

Sharcnet.ca. (n.d.). *FLUENT 6.3 User's Guide - 10.7.1 Choosing the Relative or Absolute Velocity Formulation*. [online] Available at: https://www.sharcnet.ca/Software/Fluent6/html/ug/node425.htm [Accessed 28 Apr. 2019].

Sharcnet.ca. (n.d.). *FLUENT 6.3 User's Guide - 25.4.3 Pressure-Velocity Coupling*. [online] Available at: https://www.sharcnet.ca/Software/Fluent6/html/ug/node998.htm [Accessed 1 May 2019].

Sharcnet.ca. (n.d.). *FLUENT 6.3 User's Guide - 25.9.1 Choosing the Pressure-Velocity Coupling Method*. [online] Available at: https://www.sharcnet.ca/Software/Fluent6/html/ug/node1021.htm [Accessed 1 May 2019].

Shyy, W. and Correa, S. (1985). A systematic comparison of several numerical schemes for complex flow calculations. *23rd Aerospace Sciences Meeting*.

Steers, L. and Saltzman, E. (1977). Reduced truck fuel consumption through aerodynamic design. *Journal of Energy*, 1(5), pp.312-318.

Storms, B., Satran, D., Heineck, J. and Walker, S. (2004). A Study of Reynolds Number Effects and Drag-Reduction Concepts on a Generic Tractor-Trailer. *34th AIAA Fluid Dynamics Conference and Exhibit*. [online] Available at: https://arc.aiaa.org/doi/abs/10.2514/6.2004-2251 [Accessed 13 May 2019].

Taştan, U. (2011). *Investigation of Turbulence Models used in Automotive Industry*. MSc. Middle East Technical University.

THE HIGHWAY CODE. (2015). *New higher speed limits for lorries in England and Wales*. [online] Available at: https://www.highwaycodeuk.co.uk/changes-and-answers/new-higher-speed-limits-for-lorries-in-england-and-wales# [Accessed 29 Apr. 2019].

Transportenvironment.org. (2017). *20 years of truck fuel efficiency - what progress?*. [online] Available at: https://www.transportenvironment.org/sites/te/files/2016_09_Blog_20_years_no_progress_methodological_note_final.pdf [Accessed 19 Apr. 2019].

Vanka, S. (1985). *Study of Second Order Upwind Differencing in a Recirculating Flow*. [online] National Aeronautics and Space Administration, p.2. Available at: https://ntrs.nasa.gov/archive/nasa/casi.ntrs.nasa.gov/19850021931.pdf [Accessed 2 May 2019].

Verzicco, R., Fatica, M., Iaccarino, G., Moin, P. and Khalighi, B. (2002). Large Eddy Simulation of a Road Vehicle with Drag-Reduction Devices. *AIAA Journal*, [online] 40(12), pp.2447-2455. Available at: https://arc.aiaa.org/doi/abs/10.2514/2.1613 [Accessed 13 May 2019].

Wilcox, D. (1998). *Turbulence Modeling for CFD. 2nd Edition*. La Canada, California: DCW Industries.

Wong, D. and Mair, W. (1983). Boat-tailed afterbodies of square section as drag-reduction devices. *Journal of Wind Engineering and Industrial Aerodynamics*, [online] 12(2), pp.229-235. Available at: https://www.sciencedirect.com/science/article/pii/0167610583900715 [Accessed 13 May 2019].

Yi, W. (2007). *Drag reduction of a three-dimensional car model using passive control device*. Ph.D. Seoul National University.